PIKfyve governs endoplasmic reticulum-lysosome contacts to modulate endoplasmic reticulum dynamics

Nicala Jenkins[1,2], Zainab Adamji[1,2], Nourhan R. Almasri[1], Sharifa Lomiyev[1], and Roberto J. Botelho[1,2#]

[1]Department of Chemistry and Biology and [2]Molecular Science Graduate Program, Toronto Metropolitan University, Toronto, Ontario, M5B2K3, Canada

[#]To whom correspondence should be sent: rbotelho@torontomu.ca

Running title: PIKfyve and the endoplasmic reticulum

Keywords: Lipid kinases, organelles, membrane, ER, morphology, membrane contact sites

23

24 **Abbreviations**

25 **Arl8b**: ADP-ribosylation factor like 8b; **Atg18:** autophagy-related protein 18; **ClC7:** chlorine
26 exchange transporter 7; **CLIMP63:** 63 kDa cytoskeleton linking protein; **EB1:** end-binding
27 protein 1; **ER:** endoplasmic reticulum; **FFAT**: two phenylalanine's (FF) in an acidic tract; **Fig4:**
28 factor-Induced gene 4; **FYCO1:** FYVE and coiled-coil domain autophagy adaptor 1; **FYVE**: fab1,
29 YOTB, Vac1 and EEA1 binding domain; **FYVE4A:** fab1, YOTB, Vac1 and EEA1 binding domain
30 mutant; **GFP:** green fluorescent protein; **GST:** glutathione s-transferase; **GTPase**: guanine
31 triphosphatase; **KIF5B:** kinesin-1 heavy chain isoform 5B; **LAMP1:** lysosomal associate
32 membrane protein 1; **LCR:** low complexing region; **mCherry/mCh:** monomeric cherry, red
33 fluorescent protein; **MCS:** membrane contact site; **PI(3,5)P_2**:phosphatidylinositol 3,5-
34 bisphosphate; **PI(3)P**: phosphatidylinositol 3-phosphate; **PIKfyve**: phosphoinositide FYVE-type
35 zinc finger containing; **PIP**: phosphoinositide; **PtdIns:** phosphatidylinositol; **PLA:** proximity
36 ligation assay; **PX Domain:** phox homology domain; **Rab5:** ras-related protein-5; **Rab7:** ras-
37 related protein-7; **RILP:** rab interacting lysosomal protein; **RILPC33**: rab interacting lysosomal
38 protein, c terminal 33aa fragment; **Rtn4a:** reticulon 4A; **RUFY3:** RUN and FYVE domain
39 containing 3; **RUFY4:** RUN and FYVE domain containing 4; **siRNA:** small interfering RNA; **SnxA:**
40 sorting nexin A; **Snx19:** sorting nexin 19; **TAC:** tip attachment complex; **TRPML1:** transient
41 receptor potential channel for mucolipin-1; **VAPA:** vesicle associated membrane protein-
42 associated protein A; **VAPB:** vesicle associated membrane protein-associated protein B; **VPS34:**
43 vacuolar sorting protein 34; **VPS34 In1:** vacuolar sorting protein 34 inhibitor-1

44

Summary

Lysosomes are essential to clear unwanted cellular material delivered by constant membrane fusion. Membrane fission is thus required to balance lysosome size, number, and composition. PIKfyve is a lipid kinase that converts phosphatidylinositol-3-phosphate [PtdIns(3)P] to phosphatidylinositol-3,5-bisphosphate [PtdIns(3,5)P_2] and promotes lysosome fission since lysosomes coalesce into larger, but fewer organelles in PIKfyve defective cells. Here, we reveal a role for PIKfyve in regulating endoplasmic reticulum (ER) dynamics. We show the ER is less reticulated and motile in cells acutely inhibited for PIKfyve. Partly, this arises because lysosomes cluster perinuclearly and are less motile, which appears to arrest ER hitchhiking, a process in which lysosomes pull and form ER tubules via microtubule-based movement. Secondly, the ER morphology is distorted because of hyper-tethering of protrudin, an ER transmembrane protein, to lysosomes via excess PtdIns(3)P and protrudin's FYVE domain. Thus, our findings reveal that PIKfyve activity balances phosphoinositides at ER-lysosome contact sites to govern ER properties and has significant implications to our understanding of disease linked to PIKfyve dysfunction such as neurodegeneration.

67

68

69 **Introduction**

70 Lysosomes are acidic and degradative organelles that receive and digest a plethora of molecular
71 cargo from the endocytic, autophagic and phagocytic pathways – they are thus responsible for
72 maintaining cellular homeostasis by clearing a wide variety of unwanted, damaged, and
73 potentially dangerous material (Ballabio and Bonifacino, 2020; Inpanathan and Botelho, 2019).
74 Lysosomes are highly dynamic because they continuously undergo fusion-fission cycles with
75 maturing late endosomes, transport vesicles from the *trans*-Golgi network, and between
76 themselves (Saffi and Botelho, 2019; Luzio et al., 2007). This incessant intermixing is dependent
77 on bidirectional movement of lysosomes on microtubules driven by kinesin and dynein motors
78 (Cabukusta and Neefjes, 2018). Perhaps due to this dynamic nature, lysosomes are a
79 heterogeneous collection of organelles that differ in shape, size, position, and function(Saffi
80 and Botelho, 2019; Inpanathan and Botelho, 2019). Due to this, and unless otherwise indicated,
81 we use the term *lysosomes* to encapsulate this full spectrum including late endosomes,
82 terminal lysosomes, and their hybrids, endolysosomes.

83 Given this complexity, lysosomes are subject to various regulatory inputs including by
84 the Rab7 and Arl8b GTPases and the PIKfyve lipid kinase (Ballabio and Bonifacino, 2020; Bissig
85 et al., 2017; de Lartigue et al., 2009; Cantalupo et al., 2001; Khatter et al., 2015). PIKfyve is a
86 conserved lipid kinase that localizes to endosomes and lysosomes via its FYVE domain and
87 phosphatidylinositol-3-phosphate [PtdIns(3)P], which is then converted by PIKfyve into

88 phosphatidylinositol-3,5-bisphosphate [PtdIns(3,5)P_2] (Ikonomov et al., 2001; Sbrissa et al.,
89 2002, 2007). While deletion of PIKfyve is embryonic lethal, tissue specific knockouts or
90 mutations that abate PtdIns(3,5)P_2 is associated with immunity, inflammation, metabolic
91 defects, neurological conditions and more (Ikonomov et al., 2011; Min et al., 2014; Chow et al.,
92 2007; Tsuruta et al., 2009; Cheng et al., 2025; Min et al., 2019; Prado et al., 2025). At the
93 molecular level, there remain few known PtdIns(3,5)P_2-binding proteins, which include Ca^{2+} and
94 Cl^- channels like TRPML1 and ClC7 (Leray et al., 2022; Dong et al., 2010), the actin regulator
95 cortactin (Hong et al., 2015), membrane curvature factors like the yeast Atg18 (Gopaldass et al.,
96 2017), and the *Dictyostelium* SnxA, which is proposed as a reporter for PtdIns(3,5)P_2 (Vines et
97 al., 2023). Through these and other unknown effectors, PIKfyve and PtdIns(3,5)P_2 collectively
98 control osmotic regulation, lysosome fusion-fission cycling, the degradative capacity of
99 lysosomes, and nutrient and stress sensing (Bissig et al., 2017; Choy et al., 2018; Leray et al.,
100 2022; Dong et al., 2010; Bridges et al., 2012; Sharma et al., 2019). The most glaring defect
101 caused by PIKfyve loss of function is lysosome enlargement and the concomitant decline in
102 lysosome number (Bissig et al., 2017; Choy et al., 2018; Sharma et al., 2019). This suggests that
103 PIKfyve regulates lysosome fusion-fission cycling with the evidence pointing to a specific role in
104 fission (Bissig et al., 2017; Choy et al., 2018; Sharma et al., 2019). However, the molecular
105 mechanism impacted by PIKfyve loss of function resulting in defective fission remains unclear.
106 Interestingly, endosomes and mitochondrial sites of fission are demarcated by endoplasmic
107 reticulum (ER)-dependent contacts (Friedman et al., 2013; Abrisch et al., 2020; Friedman et al.,
108 2011), but how this relates to PIKfyve and lysosomes in general is unresolved.

109 The ER is a reticulated membrane network composed of membrane sheets and tubules
110 extending throughout the cell (Westrate et al., 2015). The ER is organized into distinct
111 structural and functional domains, including the rough ER (ribosome-associated) and smooth
112 ER, that can undergo remodelling in response to stresses such as such as changes to protein
113 quality control systems involved in ER-associated degradation, protein chaperones and ER-
114 phagy (Chen et al., 2023; Goyal and Blackstone, 2013). There are several known proteins that
115 shape the ER. For example, ER sheets are formed by integral membrane proteins such as
116 CLIMP63, which forms bridge-like structures connecting opposing ER bilayers (Shibata et al.,
117 2010). In comparison, ER tubules are dynamic, continually forming, branching, and rearranging
118 through the action of proteins such as Reticulons and Atlastins (Wang et al., 2016; Hu et al.,
119 2009; Voeltz et al., 2006; Goyal and Blackstone, 2013).

120 ER remodeling can also occur through motor and cytoskeleton-driven processes. This
121 includes microtubule tip attachment complex (TAC)-mediated movement and ER-sliding, which
122 rely on the interaction between the ER membrane and microtubules to facilitate the formation
123 of new ER tubules (Waterman-Storer and Salmon, 1998; Rodríguez-García et al., 2020; Spits et
124 al., 2021), and ER hitchhiking. During ER hitchhiking, the ER forms a contact with an endosome
125 or lysosome, and the latter then moves via a microtubule and motor-dependent process
126 (Guimaraes et al., 2015; Spits et al., 2021). The attached ER then co-migrates with the motile
127 endosome/lysosome to grow a new ER tubule (Guimaraes et al., 2015; Spits et al., 2021). For ER
128 hitchhiking to occur, stable and physical contact sites between the ER and
129 endosomes/lysosomes are required (Voeltz et al., 2024). Moreover, and unlike ER-sliding and
130 TAC mediated mechanisms, which relies on direct motor attachment to the ER, hitchhiking uses

131 endosome/lysosome-motor complexes to displace the attached ER-tubules (Spits et al., 2021;
132 Raiborg et al., 2015b; a). These complexes are thought to be maintained by tethering proteins,
133 such as protrudin that bridge the two organelles together (Raiborg et al., 2015b; a; Pedersen et
134 al., 2020; Spits et al., 2021).

135 Protrudin, which was originally identified as a protein that promotes neurite formation
136 (Shirane and Nakayama, 2006), is an ER-transmembrane protein that together with VAPA,
137 another ER transmembrane protein, and the lysosomal Rab7 GTPase, form an ER-lysosome
138 tethering complex (Raiborg et al., 2015a; Pedersen et al., 2020; Matsuzaki et al., 2011; Saita et
139 al., 2009). Protrudin has a FYVE domain and a protein-binding low complexing region (LCR) that
140 respectively are thought to bind to PtdIns(3)P and GTP-bound Rab7 on endosomes/lysosomes
141 (Raiborg et al., 2015a; Pedersen et al., 2020). Protrudin then extends its cytoplasmic region to
142 loop around and interact with VAPA using the FFAT motif. Through this contact, protrudin is
143 thought to load kinesin-1 onto lysosome-bound FYCO1, a Rab7 effector that promotes
144 lysosome anterograde movement and binds PtdIns(3)P (Pedersen et al., 2020; Raiborg et al.,
145 2015a; Jongsma et al., 2024; Matsuzaki et al., 2011; Pankiv et al., 2010). Collectively, protrudin
146 not only tethers ER-lysosomes together, but also modulates their relative dynamics (Cabukusta
147 and Neefjes, 2018; Jongsma et al., 2016, 2024).

148 Overall, there is bidirectional relationship between the ER and organelles of the endo-
149 lysosomal pathway through contact sites. ER contacts appear to define areas of endosome, and
150 possibly lysosome fission, while endosomes and lysosomes help reshape ER via hitchhiking.
151 Given this, we postulated that ER-driven fission may malfunction in PIKfyve inhibition resulting

152 in lysosome coalescence. Additionally, we hypothesized that lysosome coalescence during
153 PIKfyve loss may alter ER morphology and dynamics. Here, we provide evidence that PIKfyve
154 inhibition potently distorts the ER morphology and dynamics by hindering ER hitchhiking and
155 stabilizing protrudin interaction with lysosomes via excessive PtdIns(3)P levels.

156

157 **Results**

158 *Lysosome morphology is relatively intact in cells manipulated for ER morphology*

159 PIKfyve inhibition enlarges lysosomes via coalescence, ostensibly by perturbing fission (Choy et
160 al., 2018; Bissig et al., 2017; Sharma et al., 2019). On the other hand, sites of tubular endosome
161 fission are demarcated by ER tubules that wrap around endosomes (Friedman et al., 2013;
162 Rowland et al., 2014). Conceivably then, lysosome coalescence and fission defects in PIKfyve-
163 inhibited cells may be the corollary of perturbed contacts between ER and endo-lysosomal
164 structures. To test this hypothesis, we over-expressed CLIMP63 or Rtn4A, which respectively
165 bias ER towards sheets and reticulated tubules (Shibata et al., 2010; Wang et al., 2016; Wu and
166 Voeltz, 2021; Voeltz et al., 2006), and examined their effect on lysosome morphology in resting
167 and apilimod-treated cells.

168 As expected, Cos7A cells overexpressing mCh-CLIMP63 displayed an overwhelmingly
169 sheet-like ER network with a dramatic decline of ER tubules **(Fig. 1A).** Conversely, cells
170 expressing eGFP-Rtn4 exhibited an extensive and exaggerated tubular ER network **(Fig 1B).** We
171 then quantified the average lysosome number and the average volume of individual lysosomes
172 in cells over-expressing mCherry or GFP to control for transfection, or over-expressing CLIMP63
173 or Rtn4 after incubation with apilimod to block PIKfyve. Overexpression of these proteins on

174 their own did not alter lysosome size and total lysosome number **(Fig. 1C-F).** This suggests that
175 distortion of ER morphology by these approaches does not readily change the fission-fusion
176 dynamics of dextran-loaded lysosomes. As expected, apilimod-treatment reduced lysosome
177 number and increased their size in GFP/mCherry-expressing cells (**Fig. 1C-F**). Relative to these
178 conditions, the overexpression of CLIMP63 or Rtn4 did not significantly alter the total lysosome
179 number (**Fig. 1C-F**), but they respectively enhanced and reduced apilimod-driven changes in the
180 volume of individual lysosomes **(Fig. 1D and 1F).** These results indicate that manipulating ER
181 morphology does not readily mimic the effects of PIKfyve on lysosome dynamics, and thus it is
182 unlikely that PIKfyve-regulation of lysosome fusion-fission cycling depends on ER-lysosome
183 contacts.
184
185 *PIKfyve inhibition distorts ER morphology*
186 While ER morphology had relatively minor effects on lysosome size, we next considered the
187 converse: whether lysosome distortion in PIKfyve-inhibited cells would alter the ER spatial
188 organization. To test this, we expressed ER-mNeonGreen in Cos7A cells to label the ER and
189 labelled lysosomes with a fluorescent dextran. Moreover, we opted to use a pharmacological
190 approach to block PIKfyve for these experiments because this permitted acute disturbance of
191 lysosomes, while genetic or epigenetic methods like siRNA require at least a day, which might
192 cause a host of indirect effects.
193 In vehicle-treated cells, the ER network exhibited a series of sheets and tubules throughout
194 the cell volume (**Fig 2A)**, some of which were juxtaposed to dextran-labelled lysosomes **(Fig.**
195 **2B).** Strikingly, the ER network was visibly distorted in PIKfyve-inhibited cells, exhibiting

196 numerous "black holes" **(Fig. 2A).** Many of these voids, but not all, were occupied with
197 Alexa647-dextran **(Fig. 2B).** To determine if some of these voids were also cytosolic in nature or
198 contoured by other swollen endosomal structures, we expressed cytosolic mCherry or mCherry-
199 Rab5. We found that none of the apparent ER-decorated voids labelled with cytosolic mCherry
200 (**Sup. Fig 1A**), but a subpopulation was lined with mCherry-Rab5 **(Sup. Fig 1B).** Overall, the ER
201 "black holes" were occupied with either dextran-labelled lysosomes or mCherry-Rab5
202 endosomes **(Sup. Fig 1C-D)**, indicating that separate populations of enlarged endosomal and
203 lysosomal organelles can alter the ER architecture. Similar observations were made in cells
204 inhibited with YM201636 **(Sup. Fig 2A-B).** To complement our visual inspection and buttress
205 these assertions, we quantified the ER morphology by extracting total ER skeletal length,
206 number of branches and junctions per cell, and average branch length. Apilimod and YM201636
207 both caused a significant decline in ER total skeletal length, loss of ER junctions and branch
208 numbers, though not for ER branch length **(Fig. 2C-F** and **Sup. Fig 2C-F).** Collectively, these data
209 respectively indicate a reduction in the total ER network size and loss of the ER
210 interconnectivity in cells negated for PIKfyve activity.
211
212 *Loss of PIKfyve activity impairs ER dynamics*
213 We next examined if ER motility was disturbed in PIKfyve-inhibited cells. To assess this, we
214 employed a previously described method that measures membrane displacement by tracking
215 pixel intensity changes over time (Spits et al., 2021). To achieve this, we tracked ER-
216 mNeonGreen pixels over time in control and PIKfyve-hindered cells, binning pixel displacement
217 into three categories: low (displacement of 0-3 pixels), intermediate (displacement of 4-7

218 pixels), and rapid ER movement (8 or more pixels). Relative to vehicle-treated cells, we
219 observed that cells exposed to apilimod or YM201636 displayed a greater number of pixels with
220 low membrane displacement and a corresponding drop in pixels with rapid membrane
221 displacement **(Fig. 3**; **Sup. Fig. 2A, 2G-I**; **Sup. Videos 1-3**). These results reveal that the ER is less
222 motile in cells inhibited for PIKfyve activity further reinforcing the idea that endo-lysosomal
223 coalescence distorts ER architecture and dynamics.
224
225 *ER hitchhiking is blunted in PIKfyve-perturbed cells*
226 Conceivably, the distortion of the ER spatio-temporal properties in PIKfyve-deficient cells could
227 simply arise from physical hindrance of swollen endo-lysosomes compressing the intricate ER
228 network of tubules and sheets. While physical hindrance of swollen lysosomes may very well
229 help disfigure the ER network, we noted that there were few swollen lysosomes in the
230 periphery of PIKfyve-inhibited cells (quantified below), which nevertheless sustained loss of ER
231 complexity. We thus postulated that a more sophisticated mechanism was at play.
232 The ER is partly sculpted by forming and extending new ER tubules, which can then fuse
233 with existing tubules to promote ER interconnectivity (Westrate et al., 2015; Guo et al., 2018;
234 Shibata et al., 2010; Spits et al., 2021). There are several processes that drive ER shaping that
235 depend on microtubules: ER sliding, TAC-dependent ER extension, and ER hitchhiking whereby
236 a moving endo-lysosome drags and grows a nascent ER tubule (Spits et al., 2021; Grigoriev et
237 al., 2008; Rodríguez-García et al., 2020; Guo et al., 2018; Shibata et al., 2010). We thus
238 investigated if ER spatial-temporal changes sustained in PIKfyve-inhibited cells resulted because

239 these processes were perturbed, especially in regions of the ER not physically occupied by
240 swollen endo-lysosomes.

241 First, using immunofluorescence against α-tubulin to analyze microtubule morphology,
242 we did not observe a significant difference in microtubule organization between vehicle and
243 apilimod-treated cells **(Fig. 4A)** when quantifying parameters such as number of microtubule
244 branches and junctions per cell, and average microtubule branch length **(Fig. 4B-D).** This was
245 also true for the number and kinetics of EB1-GFP comets, which associate with microtubule
246 plus-ends **(Fig. 4E-H; Sup. Videos 4-6).** We then turned to measuring ER hitchhiking events by
247 tracking ER and lysosome movement over one-minute movies at 0.3 Hz. Timelapses were then
248 analysed for lysosome-ER co-migration in control and PIKfyve-inhibited cells. We observed an
249 average of 4-6 hitchhiking events/min/100 μm^2 area in control cells, which substantially
250 dropped to 0-1 events/min/100 μm^2 in apilimod exposed cells **(Fig. 4I, J; Sup. Videos 7-8).**
251 These observations support a model whereby the botched ER morphology and dynamics in
252 PIKfyve-defective cells are partly underpinned by failed ER hitchhiking.

253

254 *Lysosome distribution and movement are altered in PIKfyve-inhibited cells*

255 Hitchhiking requires the ER to attach to a lysosome and for the lysosome to move (Spits et al.,
256 2021; Pedersen et al., 2020; Voeltz et al., 2024). We thus reasoned that abrogation of ER
257 hitchhiking in PIKfyve-hindered cells may ensue from a defect in attachment and/or lysosome
258 motility. We first tested lysosome motility and distribution in control and PIKfyve-impaired
259 cells. Using shell analysis, we reveal that lysosomes collapse into the perinuclear region and
260 become less frequent in the cell periphery **(Fig. 5A-C).** This was accompanied by a significant

261 decline in lysosome speed and total distance travelled in apilimod-treated Cos7A cells relative
262 to vehicle-treated cells (**Fig. 5E-G),** made visible through kymographs that revealed a marked
263 decrease in the motility of lysosomes upon PIKfyve inhibition (**Fig. 5D)**. Collectively, loss of
264 PIKfyve activity is associated with hindered lysosome motility and displacement to the
265 perinuclear region. This implies that in the absence of PIKfyve activity, lysosomes likely sustain a
266 loss of kinesin and/or hyperactivation of dynein activities. As a corollary, this could impair ER
267 hitchhiking and disrupt the ER network.
268
269 *PIKfyve inhibition alters ER-lysosome contact sites*
270 There are likely several types of ER-lysosome contact sites (Rudnik et al., 2024; Raiborg et al.,
271 2015a; Allison et al., 2017; Du et al., 2023; Bonet-Ponce and Cookson, 2022; Cai et al., 2022;
272 Gao et al., 2022; Saric et al., 2021). However, contact sites formed by the ER transmembrane
273 proteins, protrudin and VapA/B, and the lysosomal Rab7 GTPase, are linked to lysosome and ER
274 position and motility via kinesin (Pedersen et al., 2020; Raiborg et al., 2015a; Matsuzaki et al.,
275 2011). Therefore, we tested if PIKfyve blockade altered the protrudin-VapA-Rab7 contact site to
276 understand our earlier observations.
277 We found that protrudin and VapA appeared proximal in equal measures between
278 PIKfyve-enabled and PIKfyve-blocked cells **(Fig. 6A, E)**, which is perhaps not surprising since
279 both are ER transmembrane proteins. However, we observed an inverse relationship between
280 Rab7 and these proteins: there were fewer proximal events between VapA and Rab7 (**Fig. 6B,**
281 **F)**, but higher between protrudin and Rab7 **(Fig. 6C, G).** This did not readily translate to altered
282 Rab7 and KIF5B though (**FIG. 6D, H)**. To explore this further, we tested the status of Rab7

283 GTPase. We did not observe a change in total Rab7 associated with LAMP1 by
284 immunofluorescence (**Sup Fig. 3A-C)** in these cells and experimental conditions. Similarly, we
285 did not observe a change in the cellular levels of GTP-loaded Rab7 as reported by affinity
286 precipitation of GTP-bound Rab7 using GST-RILP-C33 in HeLa cells **(Sup Fig. 3D, E)**, though it is
287 possible that specifics pools of GTP-Rab7 may be altered in these conditions.

288 These data suggest that the Rab7-VapA-protrudin ER-lysosome contact site is
289 undergoing a reorganization rather than a complete loss, whereby protrudin-Rab7 interaction is
290 promoted at the expense of Rab7-VapA proximity**.** Since PIKfyve inhibition concomitantly
291 increases PtdIns(3)P while reducing PtdIns(3,5)P_2 levels (Choy et al., 2018; Zolov et al., 2012)
292 and protrudin has a FYVE domain, we postulated that this causes the hyper-stabilization of
293 protrudin-Rab7 interactions potentially locking ER-lysosome contact sites in a given
294 conformation.

295

296 *Lipid tethering mechanisms are altered upon PIKfyve inhibition*

297 To test the above hypothesis, we expressed GFP-chimeras of wild-type (protrudin^{wt}) and a
298 FYVE4A-mutant protrudin (protrudin^{FYVE4A}; Raiborg et al., 2015a) in cells expressing and/or
299 silenced for endogenous protrudin (**Fig. 7A**). Protrudin^{wt}-GFP and protrudin^{FYVE4A}-GFP both
300 exhibited ER-like distribution in the presence of (non-targeting) or the absence of endogenous
301 protrudin (siRNA; **Fig. 7A**). Remarkably, cells expressing protrudin^{wt}-GFP but inhibited for
302 PIKfyve displayed intense protrudin^{wt}-GFP ring structures that decorated both dextran-labelled
303 and dextran-negative vacuoles (**Fig. 7A**). Since protrudin is an ER-transmembrane protein, this
304 means that the ER membrane or regions of the ER membrane wrap around vacuoles induced in

305 PIKfyve-disabled cells. This concept is supported by 3D reconstruction of protrudin^{wt}-GFP which
306 extends and at least partially encloses dextran-loaded vacuoles (**Sup Fig. 4A**). Importantly, the
307 protrudin^{FYVE4A}-GFP mutant failed to form these rings around dextran-loaded lysosomes in
308 PIKfyve-inhibited cells (**Fig. 7A**), indicating that the protrudin-labelled ER membranes tightly
309 encircle the enlarged lysosomes likely in a PtdIns(3)P-dependent manner. Qualitative
310 observations suggests that overexpression of protrudin^{wt}-GFP, but not of the protrudin^{FYVE4A}-
311 GFP protein reduces the size of PIKfyve-induced vacuoles, reminiscent of observations when
312 cells overexpressed Rtn4a (**Fig. 1F**).

313 We then determined if excess protrudin wrapping around vacuoles was at least partially
314 responsible for the altered ER morphometrics in PIKfyve-arrested cells by skeletonizing the
315 protrudin-GFP fluorescence. First, protrudin-GFP-based ER morphometrics was
316 indistinguishable when cells were mock-silenced or silenced for endogenous protrudin (**Fig. 7B-**
317 **D**, first two groups). Second, apilimod elicited dramatic changes to ER morphometrics in cells
318 expressing wild-type protrudin-GFP whether mock or silenced for endogenous protrudin (**Fig.**
319 **7B-D**, compare groups 1 and 3, and groups 2 and 4). We then compared the ER morphometrics
320 by expressing protrudin^{FYVE4A}-GFP in cells silenced for endogenous protrudin. In vehicle-treated
321 cells, the ER morphology was similar to cells expressing protrudin^{wt}-GFP (**Fig. 7B-D**, compare
322 groups 2 and 5). Importantly, the ER changes driven by apilimod were annulled if cells
323 expressed protrudin^{FYVE4A}-GFP relative to protrudin^{wt}-GFP (**Fig. 7B-D**, compare groups 4 and 6).
324 Thus, a functional FYVE domain on protrudin was necessary for the apilimod-induced changes
325 to ER morphometrics.

326 We then explored if the absence of PtdIns(3)P or expression of protrudin^{FYVE4A}-GFP
327 rescued the relative proximity of protrudin-Rab7 and Rab7-VapA in PIKfyve-defective cells. First,
328 as a control, we note that protrudin silencing eliminated the number of proximity events
329 between Rab7-protrudin PLA (**Fig. 7E)** and Rab7-VapA PLA **(Fig.7F),** suggesting protrudin's role
330 as a contact site tether is important. Second, VPS34-IN1 which inhibits PtdIns(3)P production by
331 Vps34, reversed the excess Rab7-protrudin interactions (**Fig. 7G)** and recovered Rab7-VapA
332 interactions elicited by PIKfyve suppression (**Fig. 7H)**. This intimates that excess PtdIns(3)P in
333 PIKfyve-arrested cells reorganizes the Rab7-VapA-protrudin interactions. Third, we compared
334 the proximity of these proteins in cells expressing protrudin^{wt}-GFP or protrudin^{FYVE4A}-GFP upon
335 endogenous protrudin silencing **(Fig. 7I)**. As before, apilimod promoted Rab7-protrudin
336 interactions in cells expressing protrudin^{wt}-GFP (**Fig. 7I**). Importantly, there was no difference
337 between vehicle and apilimod treated cells expressing protrudin^{FYVE4A}-GFP (**Fig. 7I).** Even
338 expressing protrudin^{FYVE4A}-GFP alone reduced Rab7-protrudin interactions indicating that
339 protrudin-lipid interaction is important for the organization of this contact site **(Fig. 7I)**.
340 Overall, we propose that PIKfyve inhibition leads to excess PtdIns(3)P levels, which
341 inappropriately recruits and locks protrudin to lysosomes via its FYVE domain. This hyper-
342 recruitment distorts the balance of ER-lysosome contact sites by shifting interactions toward
343 Rab7-protrudin tethering and away from a conformation wherein Rab7-VapA are more
344 proximal. The disproportionate lysosomal localization of protrudin also disrupts ER morphology.
345
346 **Discussion**

347 PIKfyve is a well-established regulator of the endolysosomal pathway, governing the membrane
348 fusion-fission cycle of endosomes and lysosomes (Choy et al., 2018; Bissig et al., 2017; Sbrissa
349 et al., 2002; Ikonomov et al., 2001; Sharma et al., 2019). Here, we extend PIKfyve's sphere of
350 influence by revealing that PIKfyve modulates ER morphology and dynamics – cells acutely
351 inhibited for PIKfyve present a less reticulate and dynamic ER. Ostensibly, these changes to the
352 ER are driven partly by two mechanisms. First, the enlarged lysosomes become less motile,
353 collapsing to the cell centre – as a corollary, we observed fewer ER hitchhiking events, which
354 promotes ER remodelling and motility (Spits et al., 2021; Guimaraes et al., 2015). Second, the
355 ER membrane appears "glued" to enlarged lysosomes by extensive protrudin-dependent
356 binding, likely due to a surfeit of PtdIns(3)P (Choy et al., 2018; Zolov et al., 2012). Thus, we
357 identified an important role for PIKfyve in modulating ER properties beyond those known for
358 the endolysosomal system.
359
360 *PIKfyve modulation of lysosome and ER architecture*
361 Inhibition of PIKfyve and PtdIns(3,5)P_2 hinders lysosome fission eliciting their coalescence (Choy
362 et al., 2018; Bissig et al., 2017; Gopaldass et al., 2017; Sharma et al., 2019). Currently, we do not
363 know the fission factors controlled by PIKfyve and PtdIns(3,5)P_2 in mammalian cells, though
364 Atg18 may be such a factor in yeast (Gopaldass et al., 2017; Dove et al., 2004). On the other
365 hand, ER tubules contact and demarcate sites of mitochondrion and endosome fission
366 (Rowland et al., 2014; Friedman et al., 2013, 2011). To test if PIKfyve and ER-dependent fission
367 were linked, we overexpressed CLIMP63 and Rtn4a to respectively abate and promote ER
368 tubule formation. We reasoned that CLIMP63 overexpression would lead to enlarged

369 lysosomes, mimicking PIKfyve arrest, while excess Rtn4a might rescue lysosome coalescence in
370 PIKfyve-hindered cells by promoting ER tubules; however, we did not discern these predicted
371 behaviors. While we observed effects on individual lysosome volume in CLIMP63/Rnt4a-
372 modified cells, this was not accompanied by altered lysosome number, which intimates the
373 effects on lysosome size by CLIMP63 and Rtn4a overexpression were not because of altered
374 fusion-fission cycling, as is the case for PIKfyve (Choy et al., 2018; Sharma et al., 2019). Instead,
375 we anticipate that processes such as modified biogenesis and/or lipid transfer may drive these
376 changes to lysosome size in this context. It remains possible that CLIMP63 and Rtn4a
377 overexpression is not ideal approach to test the relationship between PIKfyve-driven processes
378 and ER.

379 Conversely, disturbing PIKfyve greatly perturbed ER morphometrics, which became less
380 reticulated and more sheet-like, decorated with various spherical voids filled with enlarged
381 lysosomes or endosomes. While some of these ER morphometric changes reflect steric
382 hindrance by the enlarged endosomes and lysosomes, our data point to a direct role for PIKfyve
383 in modulating ER properties by calibrating protrudin-dependent ER-lysosome contact sites by
384 balancing the types and levels of phosphoinositides. Supporting this model, ER morphometrics
385 were rescued in PIKfyve-arrested cells expressing the FYVE4A-protrudin mutant, but not when
386 expressing wild-type protrudin, in cells silenced for endogenous protrudin – we discuss the
387 nature of this contact further below. While physical "glueing" of the ER membrane to
388 lysosomes likely helps transform the ER morphology in PIKfyve-defective cells, we anticipate
389 that this may also directly affect ER morphogenic factors like CLIMP63, Atlastin, and reticulons
390 since protrudin interacts with these factors (Chang et al., 2013; Hashimoto et al., 2014).

391

392 *PIKfyve modulates lysosome and ER dynamics*

393 A striking consequence of PIKfyve inhibition is the concurrent loss of lysosome and ER motility,
394 which we propose are related processes. While microtubule morphometrics and dynamics
395 appeared normal in PIKfyve-inhibited cells, the enlarged lysosomes were clearly perinuclear and
396 less motile in our experimental models. While we do not precisely know how PIKfyve modulates
397 lysosome dynamics, an attractive mechanism is that PIKfyve tightly balances PtdIns(3)P and
398 PtdIns(3,5)P_2 levels in space and time to govern various PtdIns(3)P-interacting proteins such as
399 FYCO1, RUFY3, RUFY4, protrudin, and SNX19, most of which modulate motor function (Pankiv
400 et al., 2010; Saric et al., 2021; Raiborg et al., 2015a; Jongsma et al., 2024; Kumar et al., 2022;
401 Keren-Kaplan et al., 2022; Jongsma et al., 2016, 2024). Remarkably, our observations on
402 protrudin behavior align well with previous work by Saric *et al. on* SNX19, another ER
403 transmembrane protein that carries a PX domain that binds to PtdIns(3)P (Mas et al., 2014;
404 Saric et al., 2021). These authors observed that SNX19 forms an ER-lysosome contact site that
405 restricts endo-lysosome motility and that enlarged lysosomes in PIKfyve inhibited cells were
406 extensively decorated with SNX19 and were less motile (Saric et al., 2021). Collectively, we
407 propose that PIKfyve activity tightly modulates the relative levels of PtdIns(3)P and
408 PtdIns(3,5)P_2 to coordinate factors like SNX19, protrudin, FYCO1, and RUFY3/4 at ER-lysosome
409 contacts with consequences on lysosome motility. Interestingly, PIKfyve forms a conserved
410 protein complex with its antagonistic phosphatase Fig4 that back-converts PtdIns(3,5)P_2 to
411 PtdIns(3)P; it is tempting to suggest that such an antagonistic complex evolved to enable
412 exquisite control of PtdIns(3)P and PtdIns(3,5)P_2 at spatially-restricted membrane contact sites

413 to switch motor activity during bidirectional movement (Botelho et al., 2008; Jin et al., 2008;
414 Sbrissa et al., 2007; Lees et al., 2020; Botelho, 2009). This phosphoinositide-based switch may
415 interface with the previously observed role of repeated ER-endosome contacts and
416 microtubule-associated proteins in switching motor activity on endosomes (Raiborg et al.,
417 2015a; Jongsma et al., 2024)

418 As for loss of ER dynamism, we propose that this is partly due to declined lysosome
419 motility, and consequently, reduced ER hitchhiking, which is a major driver of ER remodeling
420 (Spits et al., 2021). However, ER hitchhiking also depends on the formation of lysosome-ER
421 contact sites. Based on our observations, ER-lysosome contact sites not only form, but may in
422 fact undergo hyper-tethering during PIKfyve arrest as visualized for protrudin by us and for
423 SNX19 by *Saric et al*, both of which indicate that ER membrane subdomains envelope enlarged
424 lysosomes and related organelles. This implies that bidirectional transport of lysosomes and ER
425 may depend on regulated conformational or compositional changes to these contacts which
426 consequently alter kinesin and/or dynein-mediated activity. Conceivably, PIKfyve inhibition
427 traps specific contact sites labeled with SNX19 or protrudin in a specific state arresting the
428 putative cycling necessary to elicit ER (and lysosome) dynamics.

429

430 *PIKfyve and regulation of ER-lysosome contact sites*

431 Protrudin is thought to load kinesin-1 onto FYCO1 on lysosomes (Raiborg et al., 2015a). To do
432 this, protrudin binds to PtdIns(3)P and Rab7 on lysosomes and VapA on the ER membrane
433 (Raiborg et al., 2015a). Nonetheless, there is little known about how the structural organization
434 of these proteins at these contact sites – whether all interactions are concurrent or if they are

435 subject to a regulated conformational change that enables ER and/or lysosome dynamics. Since
436 we observed an increase in protrudin-Rab7 proximity and a converse decrease in VapA-Rab7
437 proximity in PIKfyve arrested cells, this suggests that PIKfyve aids in such a
438 conformational/compositional change at this ER-lysosome contact site. Since VPS34-IN1 can
439 reverse these effects, we posit that the surplus PtdIns(3)P caused by PIKfyve inhibition locks
440 protrudin in a specific conformation that favours Rab7 and sacrifices VapA interaction. This in
441 turn may occlude Rab7 from interacting with other factors. Overall, our preferred model is that
442 PIKfyve converts PtdIns(3)P to PtdIns(3,5)P_2 to transiently promote protrudin dissociation from
443 lysosomal membrane to elicit a conformational change that promotes ER and lysosome
444 dynamics. Of course, PtdIns(3,5)P_2 itself may have a regulatory role in this process, but we do
445 not know the targets of this lipid in this context, if any. Together with effects on SNX19-
446 mediated (Saric et al., 2021) and protrudin-mediated contact sites, our results suggest that
447 PIKfyve coordinates the molecular machinery at the ER-lysosome interface, influencing both
448 organelle tethering and downstream functional outcomes such as remodeling, fission, and
449 motility.
450
451 *Conclusion*
452 Collectively, our results suggest that PIKfyve supports ER network integrity by governing
453 lysosome dynamics, distribution, and ER-lysosome contact sites. In its absence, swollen and
454 immobile lysosomes accumulate that are hyper-tethered to ER membranes in a specific
455 conformation; consequently, ER hitchhiking fails, thereby contributing to the compromised ER
456 dynamics. These results illuminate a previously underappreciated aspect of PIKfyve function

457 and provide mechanistic insight into how lysosomal dysfunction can drive architectural and
458 dynamic changes of neighboring organelles. Moreover, the PIKfyve pathway is linked to
459 neurological diseases and is a potential therapeutic target against certain cancers and viral
460 infections (Chow et al., 2007; Cai et al., 2013; Babu et al., 2024; Cheng et al., 2025; Bao et al.,
461 2023; Kang et al., 2020). The physiological link between the PIKfyve pathway and these diseases
462 is generally thought to occur through changes to the endolysosomal pathway. However, given
463 our findings, mutations in the PIKfyve pathway that lead to disease may reflect altered ER
464 function as well, particularly in highly secretory or polarized cells where proper ER architecture
465 and dynamics are critical.
466

467

468 **Methods and Materials**

469 *Cell culture*

470 COS-7 and HeLa cell strains were cultured in Dulbecco's Modified Eagle Medium (DMEM;
471 Wisent, St. Bruno, QC) supplemented with 10% heat-inactivated fetal bovine serum (FBS;
472 Wisent) and 1% penicillin-streptomycin (10,000 U/mL) (P/S; Gibco, Burlington, ON). All cells
473 were authenticated, checked for contamination and cultured at 37°C with 5% CO_2.
474

475 *Plasmids, siRNA gene silencing, and transfection*

476 Plasmids were obtained from Addgene as follows: ER-mNeonGreen (#137804), mCherry-
477 CLIMP63 (#136293), pHAGE2 GFP-Rtn4a (#86684), pcDNA3.1-mCherry (#128744), pcDNA3-
478 eGFP (#13031), human EB1 in pEGFP N1 to express EB1-GFP (#39299). Plasmids encoding

479 protrudin^{WT}-GFP, protrudin^{FYVE4A}-GFP were a kind gift from Dr. Camilla Raiborg (Oslo University
480 Hospital) and was previously described (Raiborg et al., 2015a). Transient transfections were
481 performed with FuGENE HD (Promega, Madison, WI) following the manufacturer's instructions,
482 using a 3:1 DNA to transfection reagent ratio. The transfection mixture was replaced with fresh
483 medium after 4-6 h and cells were used 24 h post-transfection.

484 Silencing RNA oligonucleotides were transfected into HeLa cells with Lipofectamine
485 RNAiMAX Transfection Reagent (Invitrogen, Carlsbad, CA) following the manufacturer's
486 instructions. One round of knockdown was performed using 25 nM ON-TARGETplus ZFYVE27
487 (the standard gene name for protrudin) individual siRNA (J-016349-12-0010) or ON-TARGETplus
488 non-targeting control (Sigma-Aldrich) over 24 h.

489

490 *Organelle labelling*

491 Lysosomes in COS-7A were labelled with 320 µg/mL Alexa-Fluor 488-, 546- or 647-conjugated
492 dextran (ThermoFisher), while lysosomes in HeLa cells were labelled with 150 µg/mL by
493 incubating cells in cell-specific complete medium for 1 h at 37°C with 5% CO_2, followed by
494 washing in phosphate-buffered saline (PBS) and replenishing with fresh complete medium for 1
495 h before live-cell imaging. Since this method likely labels a spectrum of late endosomes,
496 lysosomes and endolysosomes, the term *lysosomes* reflects this range of organelles in this
497 work. ER-NeonGreen expression was used to label bulk ER.

498

499 *Pharmacological treatments*

500 PIKfyve inhibition was accomplished by treating cells with 80-240 nM apilimod (Selleck
501 Chemicals LLC, Houston, TX) or 1 µM YM-201636 (Cayman Chemical Company, Ann Arbor, MI)
502 for 1-2 h – specific concentrations and times are indicated in each figure legend. Vps34 Class III
503 PI 3-kinase was arrested by treating cells with 1 µM VPS34-IN1 (Chemical Company, Ann Arbor,
504 MI) for 30 min.
505
506 *Immunofluorescence*
507 For immunofluorescence, following treatments, cells were fixed with 4% paraformaldehyde
508 (PFA; v/v) for 15 min. After washing with PBS, residual PFA was quenched with 100 mM glycine
509 for 10 min, then cells were blocked and permeabilized with 0.1% (v/v) Triton X-100 for 5 min.
510 Cells were then subjected to mouse monoclonal (DM1A) antibody against α-tubulin (1:100;
511 #T9026; Sigma-Aldrich), rabbit monoclonal (D9F52) antibody against Rab7 (1:100; #9367),
512 mouse monoclonal (E9O7E) antibody against Rab7 (1:100; #95746), mouse monoclonal (D4O1S)
513 antibody against LAMP1 (1:100; #15665) and rabbit monoclonal (D2D11) antibody against
514 LAMP1 (1:200; #9091; all from Cell Signaling Technology). Dylight-conjugated secondary donkey
515 antibodies against rabbit and mouse (1:1000; Novus Biologicals Canada) were used.
516
517 *Proximity ligation assays*
518 PLA was performed with Duolink In Situ Red Starter Kit Mouse/Rabbit (Sigma Aldrich,
519 DUO92101) according to the manufacturer's instructions. Briefly, HeLa cells were seeded, fixed
520 with 4% PFA for 15 min, quenched with 100 mM glycine for 10 min and permeabilized with
521 0.1% Triton X-100 for 5 min – all at RT respectively. Cells were co-incubated with one mouse

522 and one rabbit antibody from the following; rabbit monoclonal (D9F52) antibody against Rab7
523 (1:100; #9367; Cell Signaling Technology), mouse monoclonal (E9O7E) antibody against Rab7
524 (1:100; #95746; Cell Signaling Technology), mouse monoclonal (4C12) antibody against VAPA
525 (1:100; #293278; Santa Cruz Biotechnology), rabbit polyclonal antibody against ZFYVE27 (1:100;
526 12680-1-AP; Proteintech), rabbit monoclonal (E3H4J) antibody against KIF5B (1:250; #47610;
527 Cell Signaling Technology), followed by incubation with PLA probes. After probe incubation,
528 cells were washed and incubated with ligation mixtures to promote DNA ligation. Next,
529 amplification mixtures were added to cells for Rolling Circle Amplification (RCA) and
530 hybridization of fluorescently labelled oligonucleotides to occur. A PLA mounting media
531 containing DAPI was added to washed cells when mounted. PLA signals from cells were
532 detected using confocal microscopy.
533
534 *Fluorescence microscopy*
535 Confocal images were obtained using a Quorum Diskovery spinning disc confocal system
536 (Quorum Technologies, Inc., Guelph, ON) and a Quorum ReSCAN confocal system (Quorum
537 Technologies, In., Guelph, ON). The Diskovery microscope consisted of an inverted fluorescence
538 microscope (DMi8; Leica) equipped with an Andor Zyla 4.2 Megapixel sCMOS camera (Oxford
539 Instruments, Belfast, UK), a 63x oil immersion objective (1.4 NA), and standard excitation and
540 emission filter sets and lasers were used for all fluorophores. The microscope system was
541 controlled by the MetaMorph acquisition software (Molecular Devices, LLC, San Jose, CA, USA).
542 The ReSCAN microscope consisted of an inverted fluorescence microscope (DMi8 Automated;
543 Leica) equipped with a ORCA-Flash V3 digital sCMOS camera (Hamamatsu, Shizuoka Prefecture,

544 Japan) , a 63x oil immersion objective (0.6 to 1.4 NA) , and standard excitation and emission
545 filter sets and lasers were used for all fluorophores. The microscope system was controlled by
546 the Volocity acquisition software (Quorum Technologies, In., Guelph, ON). For all live-cell
547 imaging, cells were maintained in DMEM free of phenol red in a Chamlide microscope-mounted
548 chamber at 37°C and 5% CO_2. For z-stack imaging, 20-50 images were acquired with an
549 interplanar distance of 0.2 to 0.6 µm, where origin was set to the centre of the cell. For
550 timelapse obtained for ER and lysosome dynamics and EB1-GFP dynamics, frames were
551 acquired every 0.25 s for 1 min. For timelapse obtained for ER-hitchhiking, frames were
552 acquired every 0.3 s for 1 min.
553
554 *ER and lysosome morphology analysis*
555 Image analysis was conducted using Volocity and Fiji software. ER morphology analysis was
556 conducted on Volocity using an ER protocol designed to provide skeletal length measurements
557 through the thinning (or skeletonizing) of the ER until only a single-voxel-wide-line remains. The
558 protocol then counts the number of voxels along the path and provides information such as
559 skeletal length, curvature, branching and fragmentation. Further ER morphology analysis, along
560 with protrudin-GFP morphology analysis was completed using a semi-automated junction
561 analysis plug-in for Fiji provided by Spits *et al (2021)* from the Leiden University Medical Centre
562 in the Netherlands. This plug-in was based on the analyze skeleton feature on Fiji where an ER
563 mask is initially created and the skeleton representation is analyzed for the number of junctions
564 and branches (Spits et al., 2021). Lysosome morphology analysis was done on Volocity using a

565 “Measure Objects” protocol designed to provide voxel/pixel count, volume and area, and total
566 number measurements.
567
568 *ER and lysosome dynamics analysis*
569 ER dynamics were analyzed using a membrane displacement analysis macro for Fiji also
570 provided by *Spits et al (2021)* that analyzed mobile ER fractions based on #pixels/frame ranging
571 from 0-9. This method is largely based on optical flow analysis which compares corresponding
572 areas in two frames and generates a map that depicts the frame-to-frame movement of specific
573 image areas. The extent of movement is reflected by the change in pixel color intensity
574 between each frame (Spits et al., 2021). Seven separate 60-pixel x 60-pixel regions of interest
575 around the ER for one single cell per field of view were selected in a clockwise manner for
576 seven cells and the mobile ER fractions were determined. We then binned movement into
577 three categories of change (0-3 #pixels/frame), (4-7 #pixels/frame) and (8-9 #pixels/frame) to
578 define low-, intermediate-, and rapid-movement.
579 Lysosome dynamics were analyzed using Single Particle Tracking analysis for Fiji that
580 analyzed lysosome dynamics upon PIKfyve inhibition using time-lapse images acquired every
581 0.25 s for 1 min. Default settings were kept with the LoG detector (Laplacian of Gaussian). In
582 vehicle treated cells, the diameter of the lysosome was set to 1.5 µm with a quality threshold of
583 500. A uniform color was selected for color spots. The simple LAP Tracker was selected with the
584 linking max distance set to 7 µm, the gap closing distance set to 5 µm, and the gap closing max
585 frame set to 2 µm. A track index was generated, and the following parameters were extracted:
586 total distance travelled, mean speed, and overall track displacement. In PIKfyve inhibited cells,

587 the same process was followed with the exception that the diameter of the lysosome was set to
588 2 µm with a quality threshold of 250; and both the linking max distance and gap closing max
589 distance were set to 5 µm. Lysosome motility was also shown using a "Reslice" protocol in Fiji
590 to create Kymographs between conditions, where a segmented line was drawn along the x-axis
591 of the cell randomly, with a line width of 2 pixels; generating a space-time projection displaying
592 spatial position (x-axis) versus time (y-axis).

593 The frequency of ER-hitchhiking events upon PIKfyve inhibition was analyzed using
594 Time-lapse analysis acquired every 0.25 s for 1 min. Cells post-treatment were analyzed to
595 determine the number of ER-hitchhiking events for multiple, randomized (100 μm^2) regions of
596 interest (ROI). To quantify the number of events, Fiji software was utilized to select ROIs based
597 on available ER periphery with co-migrating lysosomes. A positive hitchhiking event was
598 identified if the lysosome localized with the tip of a growing ER tubule, initiated movement, co-
599 travelled with the ER tubule, and "dropped it off" at another independent ER tubule.
600 Hitchhiking events were tracked and identified qualitatively by eye.

601 *Lysosome distribution analysis*

602 To determine the change in lysosome distribution, Shell analysis on Fiji software was utilized.
603 Using the Freehand Selection Tool on Fiji, the cell was outlined to create a "total cell" ROI. This
604 was followed by using the Enlarge Tool on Fiji to create a shell by shrinking the "total cell" ROI
605 by 30-50 pixels to create a second layer of shell. This process was repeated to create a third and
606 fourth layer of shell. The raw integrated density was calculated for each shell independently to
607 determine the sum of the values of pixel intensities in the respective shell. The raw integrated

608 density of the inner most shell as a fraction of the “total cell” ROI was calculated and compared
609 to the outer most shell as a fraction of the “total cell” ROI.
610
611 *3D Image Reconstruction*
612 Three-dimensional (3D) image reconstruction was performed using Imaris Software (V9.5,
613 Bitplane, Oxford Instruments). Raw z-stack images (plane thickness: 0.2 µm) were acquired
614 using a ReSCAN Confocal Microscope (previously explained) and imported into Imaris for
615 analysis. Prior to reconstruction, image stacks were subjected to background subtraction
616 preprocessing, with a rolling ball background subtraction of 50 pixels applied across all images
617 and conditions using Fiji software. Within Imaris, 3D volumes were generated using the Surpass
618 Mode, and surfaces were rendered using the Surface or Volume modules, with thresholds set
619 manually based on signal intensity. Reconstruction parameters, including smoothing and
620 thresholding method were consistently applied across all samples to ensure comparability. For
621 visualization, coloring was applied to distinguished channels representing lysosomes (magenta)
622 and protrudin (gray).
623
624 *Recombinant protein expression and purification*
625 GST-fused RILP-C33 (truncated mutant) and GST-fused empty vectors (ampicillin resistant) were
626 expressed in BL21 competent cells, grown at 37 ºC and shaking at 200 rpm over-night . Cells
627 were cultured until the OD_{600} reached 0.6. After treatment with 1 µM isopropyl-ß-D-
628 thiogalactoside (IPTG) for 4 h at 30 ºC and shaking at 200 rpm, the induced recombinant GST-
629 RILP-C33 and GST proteins were centrifuged at 4 ºC for 30 minutes at 5000 xg, with the

630 supernatant discarded and pellet resuspended in 1X bacterial lysis buffer (50 mM Tris, 150 mM
631 NaCl, 10 mM β-mercaptoethanol, pH 7.5 with protease inhibitor cocktail (Sigma-Aldrich). The
632 bacterial lysates were then homogenized using a EmulsiFlex-C3 pressure homogenizer
633 (AVESTIN, Canada). Once homogenized, the recombinant GST-RILP-C33 and GST- lysates were
634 centrifuged at 4 ºC for 30 minutes at 5000 xg, pelleted, and the supernatant was incubated with
635 50% glutathione-Sepharose 4B bead resuspension made following manufacturer's instructions
636 (Millipore Sigma, G317-0756-01) at a dilution of 1:50 (beads to bacterial lysate supernatant,
637 respectively) for 2 h at 4 ºC with gentle shaking. The samples were then centrifuged at 4 ºC for
638 5 minutes at 5000 xg, pelleted, supernatant discarded, and pellet resuspended in 1X bacterial
639 lysis buffer. The samples were analyzed by western blotting to confirm protein expression and
640 purification.
641
642 *Affinity precipitation of GTP-bound Rab7*
643 HeLa cells were pre-treated with either vehicle control (DMSO), apilimod, or YM-201636 and
644 lysed in 700 µL modified- 1X RIPA Buffer (25 mM Tris HCl, 150 mM NaCl, 1% TritonX-100, 1% Na
645 deoxychlorate, pH 7.4 with protease inhibitor cocktail (Sigma-Aldrich)). Cells were then
646 incubated on ice for 30 minutes, collected into clean microcentrifuge tubes and centrifuged at
647 4°C for 5 minutes at 3,000 xg. Prior to centrifugation, 10% of each lysate sample was collected
648 reserved as an input control. These input samples were also centrifuged at 4°C for 5 minutes at
649 3,000 xg and subsequently mixed with a 1:1 ratio of 2X Laemmli Sample Buffer (0.5 M Tris, pH
650 6.8, glycerol and 10% sodium dodecyl sulfate (SDS), 1:10 β-mercaptoethanol). Recombinant
651 RILP-C33 and GST bound to glutathione-Sepharose 4B beads previously explained were mixed

652 with HeLa cell lysates at a dilution of 1:14 (beads to cell lysate, respectively). These mixtures
653 were incubated for 2 h at 4 ºC with gentle shaking. The samples were then centrifuged at 4°C
654 for 5 minutes at 500 xg, with remaining supernatant discarded. The sample pellets were eluted
655 using modified-1X RIPA Buffer (1:2 ratio of sample to buffer, respectively). The supernatant
656 from each wash was moved to a clean microcentrifuge tube and a 1:1 ratio of 2X Laemmli
657 Sample was added to the samples, boiled at 96°C for 10 minutes and resolved via SDS-PAGE.
658
659 *SDS-PAGE and Western blotting*
660 Following treatment, whole cell lysates were prepared in 200 µL 2x Laemmli Sample Buffer (0.5
661 M Tris, pH 6.8, glycerol and 10% SDS) supplemented with a protease and phosphatase inhibitor
662 cocktail (Complete 1x protease inhibitor (Sigma-Aldrich), Halt phosphatase inhibitor cocktail
663 (ThermoFisher Scientific). Lysates were heated at 95°C for 10 min, and 10% β-mercaptoethanol
664 and 5% bromophenol blue were added to the cell lysates. Proteins were resolved by Tris-
665 Glycine SDS-PAGE and transferred on to a polyvinylidene difluoride (PVDF) membrane. The
666 PVDF membrane was blocked for 1 h at RT in blocking buffer composed of 5% BSA in 1x final
667 Tris-buffered saline-Tween (TBS-T; 20 nM Tris, 150 mM NaCl, and 0.1% Tween-20) After
668 blocking, membranes were washed and incubated with primary antibody (at designated
669 dilution) overnight at 4°C. After primary incubation, membranes were washed and then
670 subjected to secondary antibody (at designated dilution) incubation for 1 h at RT. After
671 incubation with secondary antibody, membranes were washed and imaged using the Chemi-
672 Doc Imaging System (Bio-Rad). Western blot signals were analyzed and quantified using

673 ImageLab 6.1 (Bio-Rad). Band intensity was quantified by signal integration in an area
674 corresponding to the appropriate band.
675
676 *Statistical Analysis*
677 All experiments were performed at least three independent times with the specific total
678 number indicated in the respective figure legends along with sample size. The mean and
679 measure of variation such as standard deviation (STD) or standard error of the mean (SEM) are
680 indicated. When shown, violin plots indicate range, followed dotted lines to display 25-75%
681 percentile, the dashed line indicates median of the sampled populations. Sample means of
682 independent experiments are shown and colour coded to match the independent experiment
683 across conditions. All experimental conditions were statistically analyzed with the actual tests
684 disclosed in the respective figure legend. Unless data was normalized, sampling was assumed to
685 be normally distributed. As such, data was typically assessed with paired Student's t-test when
686 comparing two populations, with a repeated-measures one-way ANOVA for three or more
687 samples with one parameter, or repeated-measures two-way ANOVA when two parameters
688 were considered. The Geisser-Greenhouse correction was applied. Post-hoc tests were
689 employed based on assumptions and comparisons as recommended by GraphPad Prism and
690 disclosed in the respective figure legends when comparing multiple conditions in non-
691 normalized controls. ANOVA tests were coupled to Dunnett's Multiple Comparison Test for
692 one-way analysis and Tukey's multiple comparison test for two-way analysis, to analyze
693 pairwise conditions. Here, we accept $P<0.05$ as indication of statistical significance, but we
694 disclose all p values for greater transparency.

695

696 **References**

697 Abrisch, R.G., S.C. Gumbin, B.T. Wisniewski, L.L. Lackner, and G.K. Voeltz. 2020. Fission and
698 fusion machineries converge at ER contact sites to regulate mitochondrial morphology.
699 *Journal of Cell Biology*. 219. doi:10.1083/JCB.201911122.

700 Allison, R., J.R. Edgar, G. Pearson, T. Rizo, T. Newton, S. Günther, F. Berner, J. Hague, J.W.
701 Connell, J. Winkler, J. Lippincott-Schwartz, C. Beetz, B. Winner, and E. Reid. 2017.
702 Defects in ER–endosome contacts impact lysosome function in hereditary spastic
703 paraplegia. *The Journal of Cell Biology*. jcb.201609033. doi:10.1083/jcb.201609033.

704 Babu, S., K.A. Nicholson, J.D. Rothstein, A. Swenson, P.J. Sampognaro, P. Pant, E.A. Macklin, S.
705 Spruill, S. Paganoni, T.F. Gendron, M. Prudencio, L. Petrucelli, D. Nix, S. Landrette, E.
706 Nkrumah, K. Fandrick, J. Edwards, and P.R. Young. 2024. Apilimod dimesylate in C9orf72
707 amyotrophic lateral sclerosis: a randomized phase 2a clinical trial. *Brain*. 147:2998–
708 3008. doi:10.1093/brain/awae109.

709 Ballabio, A., and J.S. Bonifacino. 2020. Lysosomes as dynamic regulators of cell and organismal
710 homeostasis. *Nat Rev Mol Cell Biol*. 21:101–118. doi:10.1038/s41580-019-0185-4.

711 Bao, Y., Y. Qiao, J.E. Choi, Y. Zhang, R. Mannan, C. Cheng, T. He, Y. Zheng, J. Yu, M. Gondal, G.
712 Cruz, S. Grove, X. Cao, F. Su, R. Wang, Y. Chang, I. Kryczek, M. Cieslik, M.D. Green, W.
713 Zou, and A.M. Chinnaiyan. 2023. Targeting the lipid kinase PIKfyve upregulates surface
714 expression of MHC class I to augment cancer immunotherapy. *Proc Natl Acad Sci U S A*.
715 120:e2314416120. doi:10.1073/pnas.2314416120.

716 Bissig, C., I. Hurbain, G. Raposo, and G. van Niel. 2017. PIKfyve activity regulates reformation of
717 terminal storage lysosomes from endolysosomes. *Traffic*. 18:747–757.
718 doi:10.1111/tra.12525.

719 Bonet-Ponce, L., and M.R. Cookson. 2022. The endoplasmic reticulum contributes to lysosomal
720 tubulation/sorting driven by LRRK2. *Mol Biol Cell*. 33:ar124. doi:10.1091/mbc.E22-04-
721 0139.

722 Botelho, R.J. 2009. Changing phosphoinositides "on the fly": How trafficking vesicles avoid an
723 identity crisis. *BioEssays*. 31:1127–1136. doi:10.1002/bies.200900060.

724 Botelho, R.J., J.A. Efe, D. Teis, and S.D. Emr. 2008. Assembly of a Fab1 phosphoinositide kinase
725 signaling complex requires the Fig4 phosphoinositide phosphatase. *Mol Biol Cell*.
726 19:4273–4286. doi:10.1091/mbc.e08-04-0405.

727 Bridges, D., J.-T. Ma, S. Park, K. Inoki, L.S. Weisman, and A.R. Saltiel. 2012. Phosphatidylinositol
728 3,5-bisphosphate plays a role in the activation and subcellular localization of

729 mechanistic target of rapamycin 1. *Molecular biology of the cell*. 23:2955–62.
730 doi:10.1091/mbc.E11-12-1034.

731 Cabukusta, B., and J. Neefjes. 2018. Mechanisms of lysosomal positioning and movement.
732 *Traffic*. 19:761–769. doi:10.1111/tra.12587.

733 Cai, S., Y. Wu, A. Guillén-Samander, W. Hancock-Cerutti, J. Liu, and P. De Camilli. 2022. In situ
734 architecture of the lipid transport protein VPS13C at ER-lysosome membrane contacts.
735 *Proc Natl Acad Sci U S A*. 119:e2203769119. doi:10.1073/pnas.2203769119.

736 Cai, X., Y. Xu, A.K. Cheung, R.C. Tomlinson, A. Alcázar-Román, L. Murphy, A. Billich, B. Zhang, Y.
737 Feng, M. Klumpp, J.-M. Rondeau, A.N. Fazal, C.J. Wilson, V. Myer, G. Joberty, T.
738 Bouwmeester, M.A. Labow, P.M. Finan, J.A. Porter, H.L. Ploegh, D. Baird, P. De Camilli,
739 J.A. Tallarico, and Q. Huang. 2013. PIKfyve, a class III PI kinase, is the target of the small
740 molecular IL-12/IL-23 inhibitor apilimod and a player in Toll-like receptor signaling.
741 *Chemistry & biology*. 20:912–21. doi:10.1016/j.chembiol.2013.05.010.

742 Cantalupo, G., P. Alifano, V. Roberti, C.B. Bruni, and C. Bucci. 2001. Rab-interacting lysosomal
743 protein (RILP): The Rab7 effector required for transport to lysosomes. *EMBO Journal*.
744 20:683–693. doi:10.1093/emboj/20.4.683.

745 Chang, J., S. Lee, and C. Blackstone. 2013. Protrudin binds atlastins and endoplasmic reticulum-
746 shaping proteins and regulates network formation. *Proceedings of the National*
747 *Academy of Sciences*. 110:14954–14959. doi:10.1073/pnas.1307391110.

748 Chen, X., C. Shi, M. He, S. Xiong, and X. Xia. 2023. Endoplasmic reticulum stress: molecular
749 mechanism and therapeutic targets. *Sig Transduct Target Ther*. 8:352.
750 doi:10.1038/s41392-023-01570-w.

751 Cheng, C., J. Hu, R. Mannan, T. He, R. Bhattacharyya, B. Magnuson, J.P. Wisniewski, S. Peters,
752 S.A. Karim, D.J. MacLean, H. Karabürk, L. Zhang, N.J. Rossiter, Y. Zheng, L. Xiao, C. Li, D.
753 Awad, S. Mahapatra, Y. Bao, Y. Zhang, X. Cao, Z. Wang, R. Mehra, P. Morlacchi, V. Sahai,
754 M. Pasca di Magliano, Y.M. Shah, L.S. Weisman, J.P. Morton, K. Ding, Y. Qiao, C.A.
755 Lyssiotis, and A.M. Chinnaiyan. 2025. Targeting PIKfyve-driven lipid metabolism in
756 pancreatic cancer. *Nature*. doi:10.1038/s41586-025-08917-z.

757 Chow, C.Y., Y. Zhang, J.J. Dowling, N. Jin, M. Adamska, K. Shiga, K. Szigeti, M.E. Shy, J. Li, X.
758 Zhang, J.R. Lupski, L.S. Weisman, and M.H. Meisler. 2007. Mutation of FIG4 causes
759 neurodegeneration in the pale tremor mouse and patients with CMT4J. *Nature*. 448:68–
760 72. doi:10.1038/nature05876.

761 Choy, C.H., G. Saffi, M.A. Gray, C. Wallace, R.M. Dayam, Z.Y.A. Ou, G. Lenk, R. Puertollano, S.C.
762 Watkins, and R.J. Botelho. 2018. Lysosome enlargement during inhibition of the lipid
763 kinase PIKfyve proceeds through lysosome coalescence. *Journal of Cell Science*.
764 131:jcs213587. doi:10.1242/JCS.213587.

765 Dong, X., D. Shen, X. Wang, T. Dawson, X. Li, Q. Zhang, X. Cheng, Y. Zhang, L.S. Weisman, M.
766 Delling, and H. Xu. 2010. PI(3,5)P(2) controls membrane trafficking by direct activation
767 of mucolipin Ca(2+) release channels in the endolysosome. *Nature communications*.
768 1:38. doi:10.1038/ncomms1037.

769 Dove, S.K., R.C. Piper, R.K. McEwen, J.W. Yu, M.C. King, D.C. Hughes, J. Thuring, A.B. Holmes,
770 F.T. Cooke, R.H. Michell, P.J. Parker, and M.A. Lemmon. 2004. Svp1p defines a family of
771 phosphatidylinositol 3,5-bisphosphate effectors. *EMBO J.* 23:1922–1933.
772 doi:10.1038/sj.emboj.7600203.

773 Du, Y., W. Chang, L. Gao, L. Deng, and W.-K. Ji. 2023. Tex2 is required for lysosomal functions at
774 TMEM55-dependent ER membrane contact sites. *J Cell Biol*. 222:e202205133.
775 doi:10.1083/jcb.202205133.

776 Friedman, J.R., J.R. DiBenedetto, M. West, A.A. Rowland, and G.K. Voeltz. 2013. Endoplasmic
777 reticulum-endosome contact increases as endosomes traffic and mature. *Molecular*
778 *Biology of the Cell*. 24:1030–1040. doi:10.1091/mbc.E12-10-0733.

779 Friedman, J.R., L.L. Lackner, M. West, J.R. DiBenedetto, J. Nunnari, and G.K. Voeltz. 2011. ER
780 tubules mark sites of mitochondrial division. *Science*. 334:358–362.
781 doi:10.1126/science.1207385.

782 Gao, Y., J. Xiong, Q.-Z. Chu, and W.-K. Ji. 2022. PDZD8-mediated lipid transfer at contacts
783 between the ER and late endosomes/lysosomes is required for neurite outgrowth. *J Cell*
784 *Sci*. 135:jcs255026. doi:10.1242/jcs.255026.

785 Gopaldass, N., B. Fauvet, H. Lashuel, A. Roux, and A. Mayer. 2017. Membrane scission driven by
786 the PROPPIN Atg18. *The EMBO Journal*. 36:e201796859. doi:10.15252/embj.201796859.

787 Goyal, U., and C. Blackstone. 2013. Untangling the web: mechanisms underlying ER network
788 formation. *Biochim Biophys Acta*. 1833:2492–2498. doi:10.1016/j.bbamcr.2013.04.009.

789 Grigoriev, I., S.M. Gouveia, B. van der Vaart, J. Demmers, J.T. Smyth, S. Honnappa, D. Splinter,
790 M.O. Steinmetz, J.W. Putney, C.C. Hoogenraad, and A. Akhmanova. 2008. STIM1 is a MT-
791 plus-end-tracking protein involved in remodeling of the ER. *Curr Biol*. 18:177–182.
792 doi:10.1016/j.cub.2007.12.050.

793 Guimaraes, S.C., M. Schuster, E. Bielska, G. Dagdas, S. Kilaru, B.R.A. Meadows, M. Schrader, and
794 G. Steinberg. 2015. Peroxisomes, lipid droplets, and endoplasmic reticulum "hitchhike"
795 on motile early endosomes. *J Cell Biol*. 211:945–954. doi:10.1083/jcb.201505086.

796 Guo, Y., D. Li, S. Zhang, Y. Yang, J.-J. Liu, X. Wang, C. Liu, D.E. Milkie, R.P. Moore, U.S. Tulu, D.P.
797 Kiehart, J. Hu, J. Lippincott-Schwartz, E. Betzig, and D. Li. 2018. Visualizing Intracellular
798 Organelle and Cytoskeletal Interactions at Nanoscale Resolution on Millisecond
799 Timescales. *Cell*. 175:1430-1442.e17. doi:10.1016/j.cell.2018.09.057.

800 Hashimoto, Y., M. Shirane, F. Matsuzaki, S. Saita, T. Ohnishi, and K.I. Nakayama. 2014. Protrudin
801 regulates endoplasmic reticulum morphology and function associated with the
802 pathogenesis of hereditary spastic paraplegia. *J Biol Chem*. 289:12946–12961.
803 doi:10.1074/jbc.M113.528687.

804 Hong, N.H., A. Qi, and A.M. Weaver. 2015. PI(3,5)P2 controls endosomal branched actin
805 dynamics by regulating cortactin-Actin interactions. *Journal of Cell Biology*. 210:753–
806 769. doi:10.1083/jcb.201412127.

807 Hu, J., Y. Shibata, P.-P. Zhu, C. Voss, N. Rismanchi, W.A. Prinz, T.A. Rapoport, and C. Blackstone.
808 2009. A class of dynamin-like GTPases involved in the generation of the tubular ER
809 network. *Cell*. 138:549–561. doi:10.1016/j.cell.2009.05.025.

810 Ikonomov, O.C., D. Sbrissa, K. Delvecchio, Y. Xie, J.-P.P.J.-P. Jin, D. Rappolee, and A. Shisheva.
811 2011. The phosphoinositide kinase PIKfyve is vital in early embryonic development:
812 preimplantation lethality of PIKfyve-/- embryos but normality of PIKfyve+/- mice.
813 *Journal of Biological Chemistry*. 286:13404–13413. doi:10.1074/jbc.M111.222364.

814 Ikonomov, O.C., D. Sbrissa, and A. Shisheva. 2001. Mammalian cell morphology and endocytic
815 membrane homeostasis require enzymatically active phosphoinositide 5-kinase PIKfyve.
816 *The Journal of biological chemistry*. 276:26141–7. doi:10.1074/jbc.M101722200.

817 Inpanathan, S., and R.J. Botelho. 2019. The Lysosome Signaling Platform: Adapting With the
818 Times. *Frontiers in Cell and Developmental Biology*. 7:113. doi:10.3389/fcell.2019.00113.

819 Jin, N., C.Y. Chow, L. Liu, S.N. Zolov, R. Bronson, M. Davisson, J.L. Petersen, Y. Zhang, S. Park, J.E.
820 Duex, D. Goldowitz, M.H. Meisler, and L.S. Weisman. 2008. VAC14 nucleates a protein
821 complex essential for the acute interconversion of PI3P and PI(3,5)P(2) in yeast and
822 mouse. *The EMBO journal*. 27:3221–34. doi:10.1038/emboj.2008.248.

823 Jongsma, M.L.M., N. Bakker, L.M. Voortman, R.I. Koning, E. Bos, J.J.L.L. Akkermans, L. Janssen,
824 and J. Neefjes. 2024. Systems mapping of bidirectional endosomal transport through the
825 crowded cell. *Current Biology*. 34:4476-4494.e11. doi:10.1016/j.cub.2024.08.026.

826 Jongsma, M.L.M., I. Berlin, R.H.M. Wijdeven, L. Janssen, G.M.C. Janssen, M.A. Garstka, H.
827 Janssen, M. Mensink, P.A. van Veelen, R.M. Spaapen, and J. Neefjes. 2016. An ER-
828 Associated Pathway Defines Endosomal Architecture for Controlled Cargo Transport.
829 *Cell*. 166:152–166. doi:10.1016/j.cell.2016.05.078.

830 Kang, Y.-L., Y. Chou, P.W. Rothlauf, Z. Liu, T.K. Soh, D. Cureton, J.B. Case, R.E. Chen, M.S.
831 Diamond, S.P.J. Whelan, and T. Kirchhausen. 2020. Inhibition of PIKfyve kinase prevents
832 infection by Zaire ebolavirus and SARS-CoV-2. *Proceedings of the National Academy of*
833 *Sciences*. 202007837. doi:10.1073/pnas.2007837117.

834 Keren-Kaplan, T., A. Sarić, S. Ghosh, C.D. Williamson, R. Jia, Y. Li, and J.S. Bonifacino. 2022.
835 RUFY3 and RUFY4 are ARL8 effectors that promote coupling of endolysosomes to
836 dynein-dynactin. *Nature Communications*. 13:1506. doi:10.1038/s41467-022-28952-y.

837 Khatter, D., V.B. Raina, D. Dwivedi, A. Sindhwani, S. Bahl, and M. Sharma. 2015. The small
838 GTPase Arl8b regulates assembly of the mammalian HOPS complex on lysosomes.
839 *Journal of cell science*. 128:1746–61. doi:10.1242/jcs.162651.

840 Kumar, G., P. Chawla, N. Dhiman, S. Chadha, S. Sharma, K. Sethi, M. Sharma, and A. Tuli. 2022.
841 RUFY3 links Arl8b and JIP4-Dynein complex to regulate lysosome size and positioning.
842 *Nature Communications*. 13:1540. doi:10.1038/s41467-022-29077-y.

843 de Lartigue, J., H. Polson, M. Feldman, K. Shokat, S.A. Tooze, S. Urbé, and M.J. Clague. 2009.
844 PIKfyve regulation of endosome-linked pathways. *Traffic*. 10:883–893.
845 doi:10.1111/j.1600-0854.2009.00915.x.

846 Lees, J.A., P. Li, N. Kumar, L.S. Weisman, and K.M. Reinisch. 2020. Insights into Lysosomal
847 PI(3,5)P2 Homeostasis from a Structural-Biochemical Analysis of the PIKfyve Lipid Kinase
848 Complex. *Mol Cell*. 80:736-743.e4. doi:10.1016/j.molcel.2020.10.003.

849 Leray, X., J.K. Hilton, K. Nwangwu, A. Becerril, V. Mikusevic, G. Fitzgerald, A. Amin, M.R. Weston,
850 and J.A. Mindell. 2022. Tonic inhibition of the chloride/proton antiporter ClC-7 by
851 PI(3,5)P2 is crucial for lysosomal pH maintenance. *eLife*. 11:e74136.
852 doi:10.7554/eLife.74136.

853 Luzio, J.P., P.R. Pryor, and N.A. Bright. 2007. Lysosomes: fusion and function. *Nature reviews.*
854 *Molecular cell biology*. 8:622–632. doi:10.1038/nrm2217.

855 Mas, C., S.J. Norwood, A. Bugarcic, G. Kinna, N. Leneva, O. Kovtun, R. Ghai, L.E. Ona Yanez, J.L.
856 Davis, R.D. Teasdale, and B.M. Collins. 2014. Structural basis for different
857 phosphoinositide specificities of the PX domains of sorting nexins regulating G-protein
858 signaling. *J Biol Chem*. 289:28554–28568. doi:10.1074/jbc.M114.595959.

859 Matsuzaki, F., M. Shirane, M. Matsumoto, and K.I. Nakayama. 2011. Protrudin serves as an
860 adaptor molecule that connects KIF5 and its cargoes in vesicular transport during
861 process formation. *Mol Biol Cell*. 22:4602–4620. doi:10.1091/mbc.E11-01-0068.

862 Min, S.H., A. Suzuki, T.J. Stalker, L. Zhao, Y. Wang, C. McKennan, M.J. Riese, J.F. Guzman, S.
863 Zhang, L. Lian, R. Joshi, R. Meng, S.H. Seeholzer, J.K. Choi, G. Koretzky, M.S. Marks, and
864 C.S. Abrams. 2014. Loss of PIKfyve in platelets causes a lysosomal disease leading to
865 inflammation and thrombosis in mice. *Nature communications*. 5:4691.
866 doi:10.1038/ncomms5691.

867 Min, S.H., A. Suzuki, L. Weaver, J. Guzman, Y. Chung, H. Jin, F. Gonzalez, C. Trasorras, L. Zhao,
868 L.A. Spruce, S.H. Seeholzer, E.M. Behrens, and C.S. Abrams. 2019. PIKfyve Deficiency in

869 Myeloid Cells Impairs Lysosomal Homeostasis in Macrophages and Promotes Systemic
870 Inflammation in Mice. *Molecular and Cellular Biology*. 39. doi:10.1128/mcb.00158-19.

871 Pankiv, S., E. a. Alemu, A. Brech, J.-A.A. Bruun, T. Lamark, A. Øvervatn, G. Bjørkøy, T. Johansen,
872 A. Overvatn, G. Bjørkøy, and T. Johansen. 2010. FYCO1 is a Rab7 effector that binds to
873 LC3 and PI3P to mediate microtubule plus end - Directed vesicle transport. *Journal of*
874 *Cell Biology*. 188:253–269. doi:10.1083/jcb.200907015.

875 Pedersen, N.M., E.M. Wenzel, L. Wang, S. Antoine, P. Chavrier, H. Stenmark, and C. Raiborg.
876 2020. Protrudin-mediated ER–endosome contact sites promote MT1-MMP exocytosis
877 and cell invasion. *Journal of Cell Biology*. 219:e202003063. doi:10.1083/jcb.202003063.

878 Prado, D.S., R.T. Cattley, A.B. Sonego, P. Sutariya, S. Wu, M. Lee, W.C. Boggess, M.J. Shlomchik,
879 and W.F. Hawse. 2025. The phospholipid kinase PIKFYVE is essential for Th17
880 differentiation. *J Exp Med*. 222:e20240625. doi:10.1084/jem.20240625.

881 Raiborg, C., E.M. Wenzel, N.M. Pedersen, H. Olsvik, K.O. Schink, S.W. Schultz, M. Vietri, V. Nisi,
882 C. Bucci, A. Brech, T. Johansen, and H. Stenmark. 2015a. Repeated ER-endosome
883 contacts promote endosome translocation and neurite outgrowth. *Nature*. 520:234–8.
884 doi:10.1038/nature14359.

885 Raiborg, C., E.M. Wenzel, and H. Stenmark. 2015b. ER –endosome contact sites: molecular
886 compositions and functions. *The EMBO Journal*. 34:1848–1858.
887 doi:10.15252/embj.201591481.

888 Rodríguez-García, R., V.A. Volkov, C.-Y. Chen, E.A. Katrukha, N. Olieric, A. Aher, I. Grigoriev, M.P.
889 López, M.O. Steinmetz, L.C. Kapitein, G. Koenderink, M. Dogterom, and A. Akhmanova.
890 2020. Mechanisms of Motor-Independent Membrane Remodeling Driven by Dynamic
891 Microtubules. *Current Biology*. 30:972-987.e12. doi:10.1016/j.cub.2020.01.036.

892 Rowland, A.A., P.J. Chitwood, M.J. Phillips, and G.K. Voeltz. 2014. ER contact sites define the
893 position and timing of endosome fission. *Cell*. 159:1027–1041.
894 doi:10.1016/j.cell.2014.10.023.

895 Rudnik, S., S. Heybrock, E. Coyaud, Z. Xu, D. Neculai, B. Raught, V. Oorschot, C. Heus, J.
896 Klumperman, and P. Saftig. 2024. The lysosomal lipid transporter LIMP-2 is part of
897 lysosome-ER STARD3-VAPB-dependent contact sites. *J Cell Sci*. 137:jcs261810.
898 doi:10.1242/jcs.261810.

899 Saffi, G.T., and R.J. Botelho. 2019. Lysosome Fission: Planning for an Exit. *Trends in Cell Biology*.
900 29:635–646. doi:10.1016/j.tcb.2019.05.003.

901 Saita, S., M. Shirane, T. Natume, S.-I. Iemura, and K.I. Nakayama. 2009. Promotion of neurite
902 extension by protrudin requires its interaction with vesicle-associated membrane
903 protein-associated protein. *J Biol Chem*. 284:13766–13777.
904 doi:10.1074/jbc.M807938200.

905 Saric, A., S.A. Freeman, C.D. Williamson, M. Jarnik, C.M. Guardia, M.S. Fernandopulle, D.C.
906 Gershlick, and J.S. Bonifacino. 2021. SNX19 restricts endolysosome motility through
907 contacts with the endoplasmic reticulum. *Nat Commun*. 12:4552. doi:10.1038/s41467-
908 021-24709-1.

909 Sbrissa, D., O.C. Ikonomov, Z. Fu, T. Ijuin, J. Gruenberg, T. Takenawa, and A. Shisheva. 2007.
910 Core protein machinery for mammalian phosphatidylinositol 3,5-bisphosphate synthesis
911 and turnover that regulates the progression of endosomal transport: Novel Sac
912 phosphatase joins the ArPIKfyve-PIKfyve complex. *Journal of Biological Chemistry*.
913 282:23878–23891. doi:10.1074/jbc.M611678200.

914 Sbrissa, D., O.C. Ikonomov, and A. Shisheva. 2002. Phosphatidylinositol 3-phosphate-interacting
915 domains in PIKfyve. Binding specificity and role in PIKfyve. Endomenbrane localization.
916 *The Journal of biological chemistry*. 277:6073–9. doi:10.1074/jbc.M110194200.

917 Sharma, G., C.M. Guardia, A. Roy, A. Vassilev, A. Saric, L.N. Griner, J. Marugan, M. Ferrer, J.S.
918 Bonifacino, and M.L. DePamphilis. 2019. A family of PIKFYVE inhibitors with therapeutic
919 potential against autophagy-dependent cancer cells disrupt multiple events in lysosome
920 homeostasis. *Autophagy*. 15:1694–1718. doi:10.1080/15548627.2019.1586257.

921 Shibata, Y., T. Shemesh, W.A. Prinz, A.F. Palazzo, M.M. Kozlov, and T.A. Rapoport. 2010.
922 Mechanisms Determining the Morphology of the Peripheral ER. *Cell*. 143:774–788.
923 doi:10.1016/j.cell.2010.11.007.

924 Shirane, M., and K.I. Nakayama. 2006. Protrudin induces neurite formation by directional
925 membrane trafficking. *Science*. 314:818–821. doi:10.1126/science.1134027.

926 Spits, M., I.T. Heesterbeek, L.M. Voortman, J.J. Akkermans, R.H. Wijdeven, B. Cabukusta, and J.
927 Neefjes. 2021. Mobile late endosomes modulate peripheral endoplasmic reticulum
928 network architecture. *EMBO reports*. 22. doi:10.15252/embr.202050815.

929 Tsuruta, F., E.M. Green, M. Rousset, and R.E. Dolmetsch. 2009. PIKfyve regulates CaV1.2
930 degradation and prevents excitotoxic cell death. *Journal of Cell Biology*. 187:279–294.
931 doi:10.1083/jcb.200903028.

932 Vines, J.H., H. Maib, C.M. Buckley, A. Gueho, Z. Zhu, T. Soldati, D.H. Murray, and J.S. King. 2023.
933 A PI(3,5)P2 reporter reveals PIKfyve activity and dynamics on macropinosomes and
934 phagosomes. *Journal of Cell Biology*. 222:e202209077. doi:10.1083/jcb.202209077.

935 Voeltz, G.K., W.A. Prinz, Y. Shibata, J.M. Rist, and T.A. Rapoport. 2006. A class of membrane
936 proteins shaping the tubular endoplasmic reticulum. *Cell*. 124:573–586.
937 doi:10.1016/j.cell.2005.11.047.

938 Voeltz, G.K., E.M. Sawyer, G. Hajnóczky, and W.A. Prinz. 2024. Making the connection: How
939 membrane contact sites have changed our view of organelle biology. *Cell*. 187:257–270.
940 doi:10.1016/j.cell.2023.11.040.

Wang, S., H. Tukachinsky, F.B. Romano, and T.A. Rapoport. 2016. Cooperation of the ER-shaping proteins atlastin, lunapark, and reticulons to generate a tubular membrane network. *eLife*. 5:e18605. doi:10.7554/eLife.18605.

Waterman-Storer, C.M., and E.D. Salmon. 1998. Endoplasmic reticulum membrane tubules are distributed by microtubules in living cells using three distinct mechanisms. *Current Biology*. 8:798–807. doi:10.1016/S0960-9822(98)70321-5.

Westrate, L.M., J.E. Lee, W.A. Prinz, and G.K. Voeltz. 2015. Form follows function: the importance of endoplasmic reticulum shape. *Annu Rev Biochem*. 84:791–811. doi:10.1146/annurev-biochem-072711-163501.

Wu, H., and G.K. Voeltz. 2021. Reticulon-3 Promotes Endosome Maturation at ER Membrane Contact Sites. *Developmental Cell*. 56:52-66.e7. doi:10.1016/j.devcel.2020.12.014.

Zolov, S.N., D. Bridges, Y. Zhang, W.-W. Lee, E. Riehle, R. Verma, G.M. Lenk, K. Converso-Baran, T. Weide, R.L. Albin, A.R. Saltiel, M.H. Meisler, M.W. Russell, and L.S. Weisman. 2012. In vivo, Pikfyve generates PI(3,5)P2, which serves as both a signaling lipid and the major precursor for PI5P. *Proceedings of the National Academy of Sciences of the United States of America*. 109:17472–7. doi:10.1073/pnas.1203106109.

Funding

RJB was a recipient of a Canada Research Chair (#950-232333) with contributions from Toronto Metropolitan University and Faculty of Science. The Natural Sciences and Engineering Research Council (NSERC) of Canada funded this research with Discovery research grant to RJB (RGPIN-2020-04343). NRA was partly funded by an NSERC Undergraduate Student Research

Award. Canada Foundation for Innovation with contributions from the Ministry of Training, Colleges, and Universities of Ontario and from Toronto Metropolitan supported this work with John Evans Leadership Fund to RJB (#32957 and #38151).

Acknowledgements

We would like to thank Dr. Camilla Raiborg (Oslo University Hospital) for kindly providing the plasmids encoding the GFP fusion of the wild-type and of the FYVE4A mutant of protrudin. We also thank Kimberly Lau at the Sick Kids Imaging Facility for advise on Imaris and 3D reconstruction.

Figure Legends

Figure 1: Overexpression of ER morphogenic proteins does not readily mimic PIKfyve inhibition in COS-7A cells. (A, B) Confocal images of COS-7A cells labeled with Dextran, Alexa Fluor-488 (magenta) and transiently expressing mCh-CLIMP63/mCherry (gray) (A) or Alexa Fluor-546 expressing eGFP-Rtn4a/eGFP (gray) (B). Cells were exposed to either 0.01% vehicle (DMSO) or 80 nM apilimod for 2 h. **(C-D)** Quantification of lysosome number and volume upon

991 expression of CLIMP63 to induce ER sheets. **(E-F)** Quantification of lysosome number and
992 volume upon expression of Rtn4a to promote ER tubulation. Scale bar = 20 µm . All experiments
993 were repeated four independent times. Data points from matching independent experiments
994 are color coded. Shown is the mean ± SEM. Data are based on 30-50 transfected cells per
995 condition per experiment. Data was analyzed using repeated measures two-way ANOVA and
996 Tukey's multiple comparisons test and p values are shown.
997
998 **Figure 2: PIKfyve loss of function alters the ER morphology. (A, B)** Confocal images of COS-7A
999 cells transiently transfected with ER-mNeonGreen (gray), labeled with Dextran, Alexa Fluor 647
1000 (magenta), and treated with 0.01% vehicle (DMSO) or 80 apilimod for 2 h. Skeletonize function
1001 was applied respectively to trace ER morphology (A). **(C-F)** Quantification of ER morphology
1002 including ER skeletal length (C), number of ER junctions per cell (D), number of branches per cell
1003 (E), and average branch length (µm) (F). Scale bar: full size = 20 µm, zoom insert = 5 µm. All
1004 experiments were repeated four independent times. Data points from matching independent
1005 experiments are colour coded. Shown is the mean ± SEM. Data are based on 15-20 transfected
1006 cells per condition per experiment. Data was analyzed using a two-tailed paired Student's t-test
1007 and p values are shown.
1008
1009 **Figure 3: ER motility is reduced in PIKfyve inhibited cells. (A)** Representative time-lapse
1010 confocal images of COS-7A cells transiently transfected with ER-mNeonGreen (gray). Zoom
1011 inserts show ER redistribution as indicated by the white arrow. Cells were exposed to either
1012 0.02% vehicle (DMSO) or 240 nM apilimod for 2 h. **(B-D)** Quantification of membrane

1013 displacement analysis categorized by low movement (B), intermediate movement (C), and rapid
1014 movement (D). Scale bar: full size = 20 µm, zoom insert = 5 µm. All experiments were repeated
1015 five independent times. Data points from matching independent experiments are colour coded.
1016 Shown is the mean ± SEM. Data are based on 7 randomized ROIs for 7-10 transfected cells, per
1017 condition per experiment. Data was analyzed using a two-tailed paired Student's t-test and p
1018 values are shown.
1019
1020 **Figure 4. ER-remodeling via hitchhiking is reduced upon PIKfyve inhibition. (A)** Confocal
1021 images of HeLa cells immunostained for α-tubulin (gray) treated with 0.02% vehicle (DMSO),
1022 240 nM apilimod or 1 µM YM-201636 for 2 h. **(B-D)** Quantification of microtubule morphology
1023 including number of branches per cell (B), number of junctions per cell (C), and average branch
1024 length (D). For B through D, all experiments were repeated four independent times. **(E)**
1025 Confocal images of COS-7A cells transiently transfected with EB1-GFP displayed as Rainbow
1026 RBG LUT and treated as in A. **(F-H)** Semi-quantification of microtubule dynamics including
1027 percentage of cells with >10 EB1-puncta (F), percentage of cells with mobile EB1-puncta (G),
1028 and percentage of cells with EB1-puncta moving away from the nucleus (H). For F-H, all
1029 experiments were repeated three independent times. For B-D and F-H, data was analyzed using
1030 an Ordinary one-way ANOVA test and Dunnett's multiple comparisons test. **(I)** Quantification of
1031 the number of ER-hitchhiking events that occurred in a 100 μm^2 ROI over one minute, repeated
1032 three independent times. **(J)** Confocal images of COS-7A cells transiently transfected with ER-
1033 mNeonGreen (gray) and labeled with Dextran, Alexa Fluor 647 (magenta) and exposed to either
1034 0.02% vehicle (DMSO) or 240 nM apilimod. Zoom inserts show an ER-hitchhiking event

1035 occurring over 2.5 seconds as indicated by the white arrow. Data were analyzed using a two-
1036 tailed paired Student's t-test and p values are shown. Data points from matching independent
1037 experiments are color coded. Shown is the mean ∓ SEM. Scale bar: full size = 20 µm, zoom
1038 insert = 5 µm. P values are shown.
1039
1040 **Figure 5. PIKfyve activity supports lysosome mobility and spatial distribution. (A)** Confocal
1041 images of COS-7A cells labeled with Dextra, Alexa Fluor 647 (magenta) and exposed to either
1042 0.02% vehicle (DMSO) or 240 nM apilimod for 2 h. Scale bar = 20 µm. **(B)** Schematic
1043 representation of the changes to lysosome spatial distribution between control and PIKfyve
1044 inhibited conditions. **(C)** Quantification of the distribution of lysosomes in the perinuclear
1045 region versus the peripheral region of the cell. A ratio of the number of lysosomes in the
1046 perinuclear region to total number of lysosomes in the cell was determined – the same was
1047 done for the peripheral region respectively. **(D)** Kymograph of lysosome movement along a
1048 linear ROI. The vertical axis represents time (s), and the horizontal axis represents distance
1049 along a selected path. Diagonal or segmented lines indicate motility; vertical lines represent
1050 stationary organelles. **(E-G)** Quantification of lysosome motility including track mean speed (E),
1051 total distance travelled (F), and track displacement (G). All experiments were repeated four
1052 independent times. Data points from matching independent experiments are colour coded.
1053 Shown is the mean ± SEM. Data were analyzed using a two-way ANOVA and Tukey's multiple
1054 comparison test for (C) and two-tailed paired Student's t-test for (E-G) and p values are shown.
1055

1056 **Figure 6. Loss of PIKfyve activity alters Protrudin-VapA-Rab7 ER-lysosome contact site. (A-D)**
1057 Confocal images of HeLa cells treated with 0.02% vehicle (DMSO), 240 nM apilimod, or 1 µM
1058 YM-201636 for 2 h followed by Proximity Ligation Assay between protrudin and VapA (A), or
1059 Rab7 and VapA (B), or Rab7 and protrudin (C), or Rab7 and Kinesin-1 (KIF5B; D). Images were
1060 generated by maximum projection of z-stacks of the PLA signal (magenta); DAPI-stained nucleus
1061 is shown in gray. Negative controls where one of the primary antibodies was missing are
1062 shown. Scale bar = 15 µm. **(E-H)** Quantification of the number of PLA dots per cell for each
1063 protein pair tested in A-D, as indicated in image. All experiments were repeated four
1064 independent times with matching independent experiments colour coded. Shown is the mean
1065 $\pm$ SEM. Data were analyzed using an Ordinary one-way ANOVA and Dunnett's multiple
1066 comparisons test and p values are shown.
1067
1068 **Figure 7. Protrudin hyper-tethers ER and lysosomes during PIKfyve inhibition to alter ER**
1069 **morphology. (A)** Confocal images of HeLa cells co-transfected with non-targeting siRNA control
1070 or siRNA oligonucleotides against protrudin, and protrudin^{wt}-GFP or protrudin^{FYVE4A}-GFP (gray).
1071 Cells were labeled with Dextran, Alexa 546 (magenta) and then exposed to either 0.02% vehicle
1072 (DMSO) or 240 nM apilimod for 2 h. Scale bar: full size = 20 µm, zoom insert = 5 µm. **(B-D)**
1073 Quantitative analysis of ER morphology based on protrudin^{wt}-GFP or protrudin^{FYVE4A}-GFP
1074 fluorescence in conditions shown in A: number of protrudin branches per cell (B), junctions per
1075 cell (C), and average branch length (D). **(E, F)** Quantification of number of PLA dots between
1076 Rab7 and protrudin (E) and Rab7 and VapA (F) in control silenced and protrudin-silenced cells
1077 with and without apilimod. **(G, H)** Quantification of PLA dots between Rab7 and protrudin (G)

1078 and Rab7-VapA (H) in cells treated with vehicle, apilimod, or Vps34-IN to abate PtdIns(3)P
1079 levels. **(I)** Quantification of PLA dots between Rab7 and protrudin in mock-silenced or
1080 protrudin-silenced cells expressing protrudin^{wt}-GFP or protrudin^{FYVE4A}-GFP exposed to either
1081 vehicle or apilimod. All experiments were repeated three independent times and colour-code
1082 matched. Shown is the mean $\pm$ SEM. Data for (B-F) and (I) were analyzed using two-way
1083 ANOVA and Tukey's multiple comparison test; Data for (G-H) were analyzed using a one-way
1084 ANOVA and Tukey's multiple comparison test. P values are shown.
1085
1086 **Supplementary Figure Legend**
1087 **Supplementary Figure 1. Voids in ER architecture are filled with vacuolated endosomes and**
1088 **lysosomes upon PIKfyve inhibition. (A-B)** Confocal images of COS-7A cells labeled with Dextran,
1089 Alexa Fluor 647 (magenta) and transiently expressing ER-mNeonGreen (gray) or mCherry (cyan)
1090 (A) or mRFP-Rab5 (cyan) (B). Cells were exposed to either 0.01% DMSO or 80 nM apilimod for 2
1091 h. Scale bar: full size = 20 µm, zoom insert = 5 µm. **(C-D)** Quantification of Mander's Analysis
1092 done on the colocalization between Dextra, Alexa 647 and mRFP-Rab5. All experiments were
1093 repeated three independent times. Data points from matching independent experiments are
1094 colour coded and shown as mean $\pm$ SEM from 30-50 transfected cells per condition per
1095 experiment. Data were analyzed using a two-tailed Students t-test and p values are shown.
1096
1097 **Supplementary Figure 2. ER morphology and dynamics are altered upon PIKfyve inhibition**
1098 **using YM-201636. (A)** Representative time-lapse confocal images of COS-7A cells transiently
1099 transfected with ER-mNeonGreen (gray). Zoom inserts show ER redistribution as indicated by

1100 the white arrow and Skeletonize function was applied respectively to trace ER morphology. **(B)**
1101 Confocal images of COS-7A cells transiently transfected with ER-mNeonGreen (gray) and
1102 labelled with Dextran, Alexa-647 (magenta). Cells were exposed to either 0.02% vehicle (DMSO)
1103 or 1 µM YM-201636 for 2 h. Scale bar: full size = 20 µm, zoom insert = 5 µm. **(C-F)**
1104 Quantification of ER morphology including ER skeletal length (C), number of ER junctions per
1105 cell (D), number of branches per cell (E), and average branch length (F). **(G-I)** Quantification of
1106 membrane displacement analysis categorized by low movement (G), intermediate movement
1107 (H), and rapid movement (I). Experiments (C-F) were repeated four independent times;
1108 Experiments (G-I) were repeated six independent times. Data points from matching
1109 independent experiments are colour coded. Shown in the mean ± SEM. Data from C through F
1110 are based on 15-20 transfected cells per condition per experiment. Data from G through I are
1111 based on 7 randomized ROIs for 7-10 transfected cells, per condition per experiment. Data
1112 were analyzed using a two-tailed Student's t-test and p values are shown.
1113
1114 **Supplementary Figure 3. Upon PIKfyve inhibition Rab7 GTPase status appears unaltered. (A)**
1115 HeLa cells immuno-stained for LAMP1 (magenta) and Rab7 (gray) following treatment with
1116 0.02% vehicle (DMSO) and 240 nM apilimod for 2 h. **(B-C)** Quantitative analysis displaying the
1117 average Mander's Coefficient for the fraction of Rab7 colocalized with LAMP1 (B), and fraction
1118 of LAMP1 colocalized with Rab7 (C). **(D)** Representative Western blots of affinity purification of
1119 Rab7-GTP using GST-RILPC33, displaying total Rab7 levels from input samples and GTP-Rab7
1120 levels recovered with the GST negative control and GST-RILPC33 from cells exposed to 0.02%
1121 vehicle (DMSO), 240 nM apilimod or 1 µM YM-201636 for 2 h. **(E)** Quantitative analysis of

1122 affinity precipitated GTP-Rab7 from GST negative control and GST-RILPC33. GST-control and
1123 GST-RILPC33 were normalized first to input levels of β-actin and then Rab7. All experiments
1124 were repeated three independent times. Data points from matching independent experiments
1125 are colour coded and shown as the mean ± STD. Data from B through C was analyzed using a
1126 two-tailed Student's t-test. Data from E was analyzed using a two-way ANOVA and Tukey's
1127 multiple comparisons test and p values are shown.

1128

1129 **Supplementary Figure 4. Three-dimensional reconstruction of protrudin-positive ER. (A)**
1130 Three-dimensional reconstruction of HeLa cells co-transfected with non-targeting siRNA control
1131 or siRNA oligonucleotides against protrudin, and expressing protrudin^{wt}-GFP or protrudin^{FYVE4A}-
1132 GFP (gray). Cells were labeled with Dextran, Alexa 546 (magenta) and then exposed to either
1133 0.02% vehicle (DMSO) or 240 nM apilimod for 2 h. Scale bar: full frame = 20 µm, zoom insert =
1134 0.7 µm. **(B)** Representative Western blots of non-targeting siRNA control or siRNA
1135 oligonucleotides against protrudin displaying protrudin and clathrin levels. **(C)** Quantitative
1136 analysis displaying protrudin protein levels upon transfection with siNT or siProtrudin after
1137 normalized to loading control, clathrin. All experiments were repeated three independent
1138 times. Data points from matching independent experiments are colour coded. Shown in the
1139 mean ± STD. Data was analyzed using a two-tailed Student's t-test and p values are shown.

1140

1141 **Supplementary Video Legend**

1142 **Supplemental Video 1. ER motility is retained upon treatment with vehicle control (DMSO).**
1143 COS-7A cells were transiently transfected with ER-mNeonGreen (gray) and treated with 0.02%

1144 vehicle (DMSO) for 2 h. The ER network undergoes continuous remodeling through tubule
1145 extension, retraction, and branching, reflecting its highly dynamic and interconnected nature.
1146 Time-lapse images were acquired at a rate of 4 frame/s for 1 minute. Still frames from Video 1
1147 are displayed in Figure 3A. Scale bar: 20 µm.
1148
1149 **Supplemental Video 2. ER motility is reduced upon acute treatment with PIKfyve inhibitor**
1150 **Apilimod.** COS-7A cells were transiently transfected with ER-mNeonGreen (gray) and treated
1151 with 240 nM apilimod for 2 h. Time-lapse images were acquired at a rate of 4 frame/s for 1
1152 minute. Still frames from Video 2 are displayed in Figure 3A. Scale bar: 20 µm.
1153
1154 **Supplemental Video 3. ER motility is reduced upon acute treatment with PIKfyve inhibitor**
1155 **YM-201636.** COS-7A cells were transiently transfected with ER-mNeonGreen (gray) and treated
1156 with 1 µM YM-201636 for 2 h. Time-lapse images were acquired at a rate of 4 frame/s for 1
1157 minute. Still frames from Video 3 are displayed in Supplemental Figure 2A. Scale bar: 20 µm.
1158
1159 **Supplemental Video 4. EB1-GFP dynamics under vehicle condition conditions.** COS-7A cells
1160 were transiently transfected with EB1-GFP displayed as a rainbow LUT scale, where red is the
1161 highest intensity level and blue is the lowest intensity level. Cells were treated with 0.02%
1162 vehicle (DMSO) for 2 h. EB1-GFP comets mark the plus-ends of growing microtubules, enabling
1163 visualization of dynamic microtubules. Time-lapse images were acquired at a rate of 4 frame/s
1164 for 1 minute. Still frames from Video 4 are displayed in Figure 4E. Scale bar: 20 µm.
1165

1166 **Supplemental Video 5. EB1-GFP dynamics appear unaltered upon PIKfyve inhibition using**
1167 **apilimod.** COS-7A cells were transiently transfected with EB1-GFP displayed as a rainbow LUT
1168 scale, where red is the highest intensity level and blue is the lowest intensity level. Time-lapse
1169 images were acquired at a rate of 4 frame/s for 1 minute. Still frames from Video 5 are
1170 displayed in Figure 4E. Scale bar: 20 µm.
1171
1172 **Supplemental Video 6. Microtubule EB1 dynamics remain unaffected by YM-201636**
1173 **treatment.** COS-7A cells were transiently transfected with EB1-GFP displayed as a rainbow LUT
1174 scale, where red is the highest intensity level and blue is the lowest intensity level. Time-lapse
1175 images were acquired at a rate of 4 frame/s for 1 minute. Still frames from Video 6 are
1176 displayed in Figure 4E. Scale bar: 20 µm.
1177
1178 **Supplemental Video 7. Normal ER-movement via organelle hitchhiking in vehicle-treated**
1179 **cells.** COS-7A cells were transiently transfected with ER-mNeonGreen (gray) and labeled with
1180 Dextran, Alexa 647 (magenta) followed by treatment with 0.02% vehicle (DMSO) for 2 h.
1181 Positive hitchhiking events were scored based on ER movement driven by physical association
1182 with a motile dextran labelled lysosome. Timelapse images were acquired at a rate of 3.3
1183 frames/s for 1 minute. Still frames from Video 7 are displayed in Figure 4J. Scale bar: 20 µm.
1184
1185 **Supplemental Video 8. ER-hitchhiking frequency drops upon PIKfyve inhibition.** COS-7A cells
1186 were transiently transfected with ER-mNeonGreen (gray) and labeled with Dextran, Alexa 647
1187 (magenta) followed by treatment with 240 nM apilimod for 2 h. Positive hitchhiking events

1188 were scored based on ER movement driven by physical association with a motile dextran

1189 labelled lysosome. Timelapse images were acquired at a rate of 3.3 frames/s for 1 minute. Still

1190 frames from Video 7 are displayed in Figure 4J. Scale bar: 20 µm.

1191

FIGURE 1.

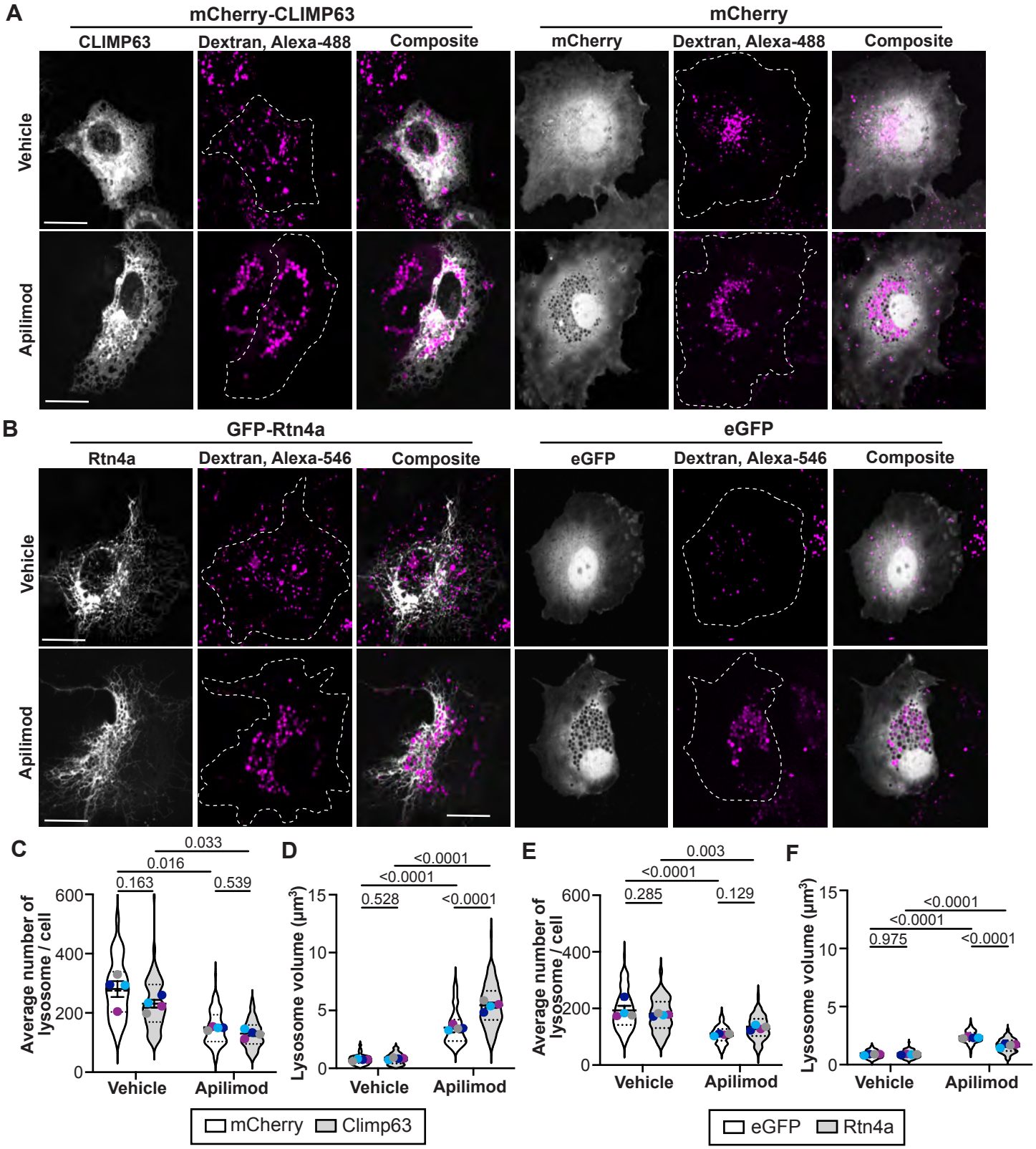
A
mCherry-CLIMP63
mCherry
CLIMP63
Dextran, Alexa-488
Composite
mCherry
Dextran, Alexa-488
Composite
Vehicle
Apilimod
B
GFP-Rtn4a
eGFP
Rtn4a
Dextran, Alexa-546
Composite
eGFP
Dextran, Alexa-546
Composite
Vehicle
Apilimod
C
Average number of lysosome / cell
0.033
0.016
0.163
0.539
Vehicle
Apilimod
D
Lysosome volume (µm³)
<0.0001
<0.0001
0.528
<0.0001
Vehicle
Apilimod
E
Average number of lysosome / cell
0.003
<0.0001
0.285
0.129
Vehicle
Apilimod
F
Lysosome volume (µm³)
<0.0001
<0.0001
0.975
<0.0001
Vehicle
Apilimod
mCherry
Climp63
eGFP
Rtn4a

FIGURE 2.

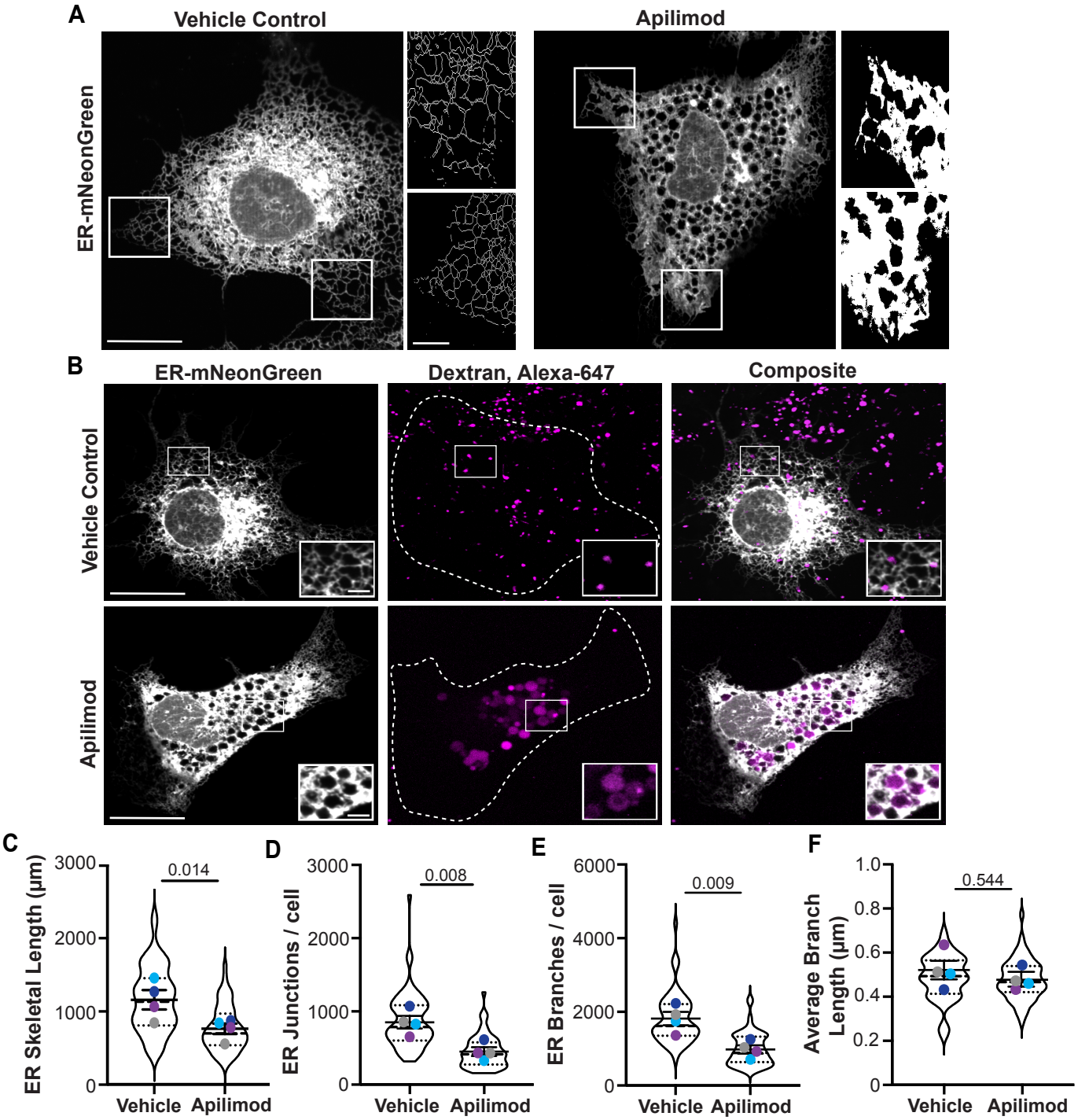
A
Vehicle Control
Apilimod
ER-mNeonGreen
B
ER-mNeonGreen
Dextran, Alexa-647
Composite
Vehicle Control
Apilimod
C
ER Skeletal Length (µm)
3000
2000
1000
0
0.014
Vehicle
Apilimod
D
ER Junctions / cell
3000
2000
1000
0
0.008
Vehicle
Apilimod
E
ER Branches / cell
6000
4000
2000
0
0.009
Vehicle
Apilimod
F
Average Branch Length (µm)
1.0
0.8
0.6
0.4
0.2
0
0.544
Vehicle
Apilimod

FIGURE 3.

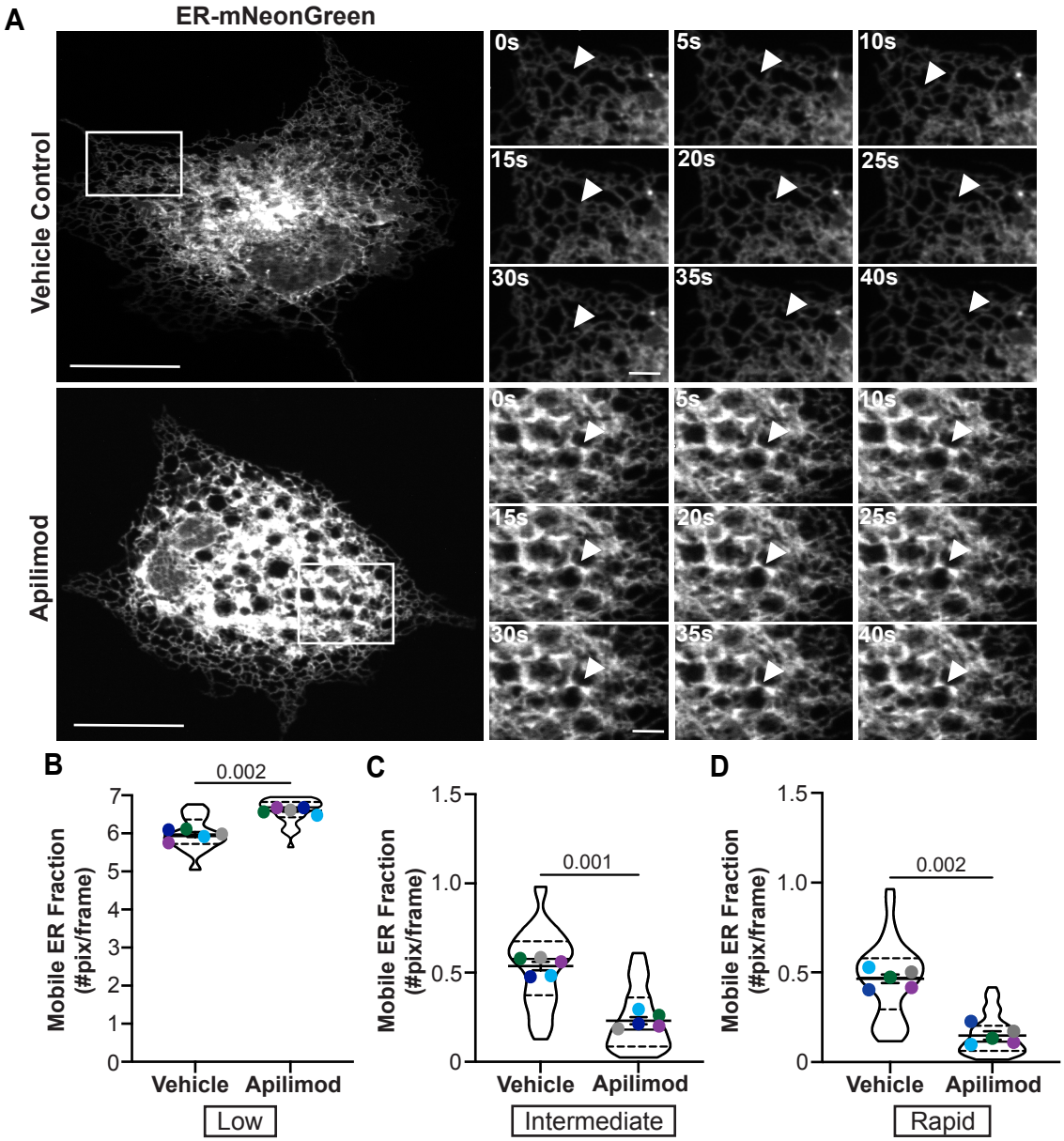
A
ER-mNeonGreen
Vehicle Control
Apilimod
0s
5s
10s
15s
20s
25s
30s
35s
40s
B
C
D
Mobile ER Fraction (#pix/frame)
0.002
0.001
0.002
Vehicle
Apilimod
Low
Intermediate
Rapid

FIGURE 4.

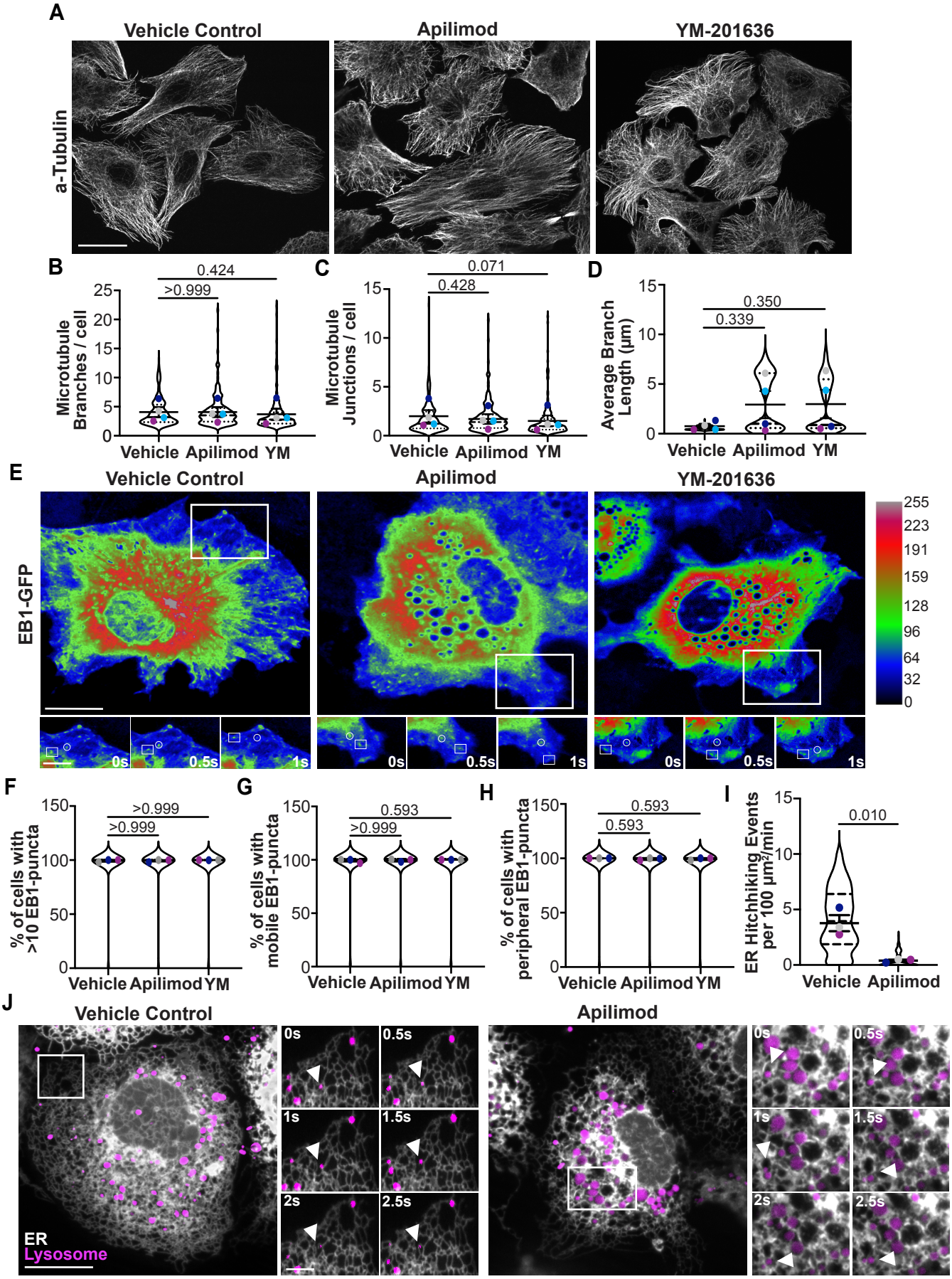
A
Vehicle Control
Apilimod
YM-201636
a-Tubulin
B
Microtubule Branches / cell
0.424
>0.999
Vehicle Apilimod YM
C
Microtubule Junctions / cell
0.071
0.428
Vehicle Apilimod YM
D
Average Branch Length (µm)
0.350
0.339
Vehicle Apilimod YM
E
Vehicle Control
Apilimod
YM-201636
EB1-GFP
255
223
191
159
128
96
64
32
0
0s
0.5s
1s
F
% of cells with >10 EB1-puncta
>0.999
>0.999
Vehicle Apilimod YM
G
% of cells with mobile EB1-puncta
0.593
>0.999
Vehicle Apilimod YM
H
% of cells with peripheral EB1-puncta
0.593
0.593
Vehicle Apilimod YM
I
ER Hitchhiking Events per 100 µm²/min
0.010
Vehicle Apilimod
J
Vehicle Control
Apilimod
ER
Lysosome
0s
0.5s
1s
1.5s
2s
2.5s

FIGURE 5.

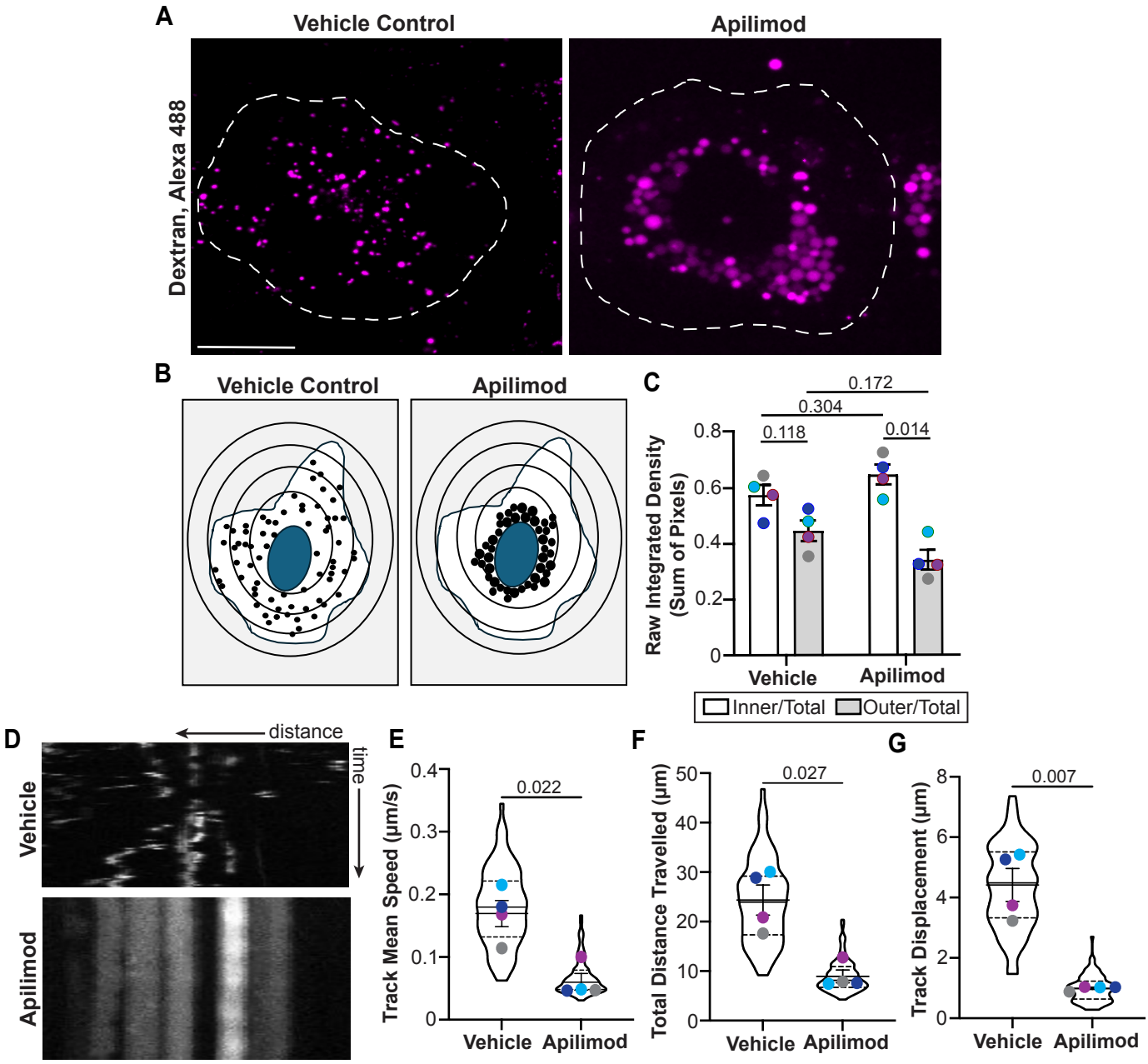
A
Vehicle Control
Apilimod
Dextran, Alexa 488
B
Vehicle Control
Apilimod
C
0.172
0.304
0.118
0.014
Raw Integrated Density (Sum of Pixels)
0.8
0.6
0.4
0.2
0
Vehicle
Apilimod
Inner/Total
Outer/Total
D
distance
time
Vehicle
Apilimod
E
0.022
Track Mean Speed (µm/s)
0.4
0.3
0.2
0.1
0
Vehicle
Apilimod
F
0.027
Total Distance Travelled (µm)
50
40
30
20
10
0
Vehicle
Apilimod
G
0.007
Track Displacement (µm)
8
6
4
2
0
Vehicle
Apilimod

FIGURE 6.

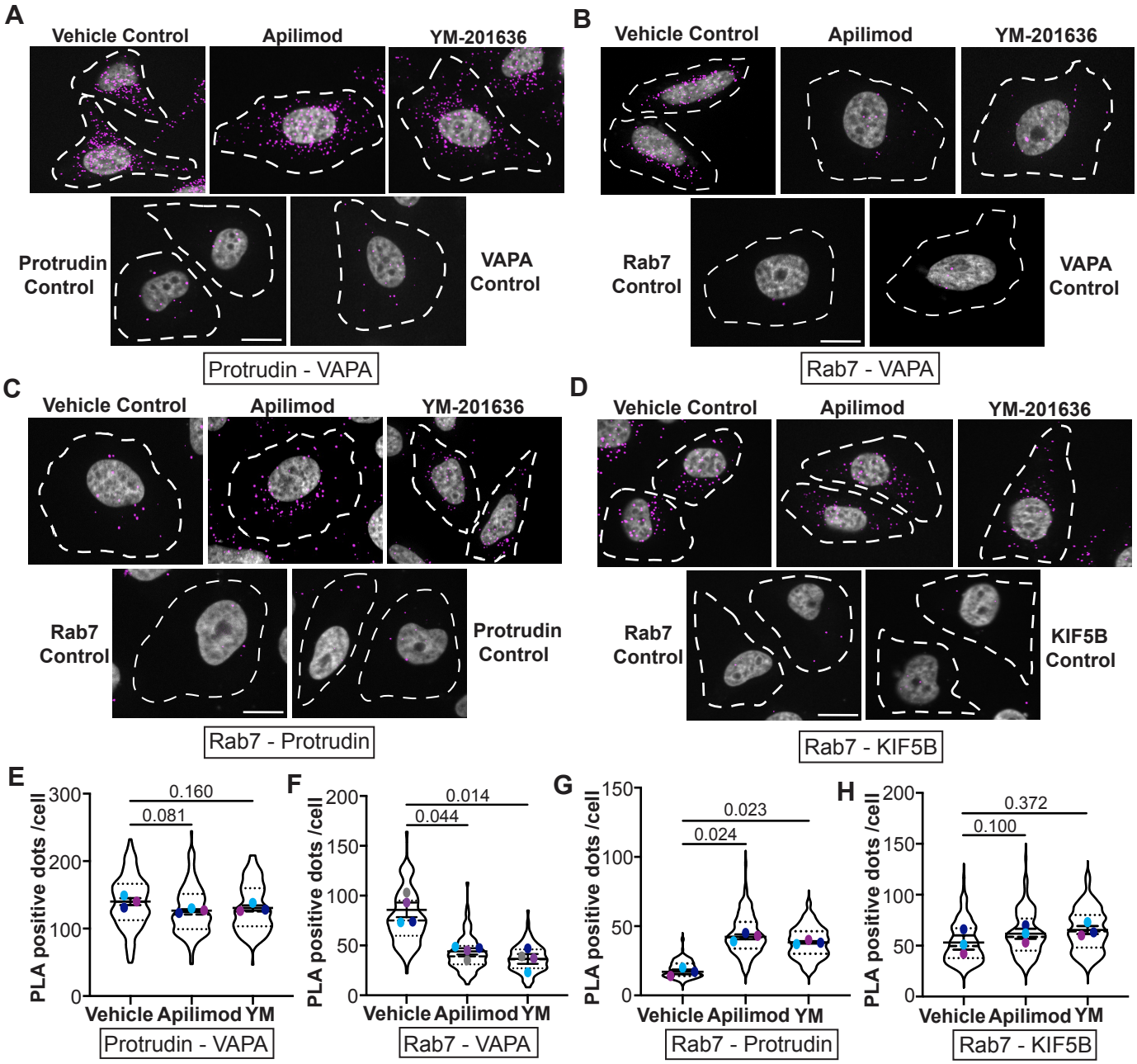
A
Vehicle Control
Apilimod
YM-201636
Protrudin Control
VAPA Control
Protrudin - VAPA
B
Vehicle Control
Apilimod
YM-201636
Rab7 Control
VAPA Control
Rab7 - VAPA
C
Vehicle Control
Apilimod
YM-201636
Rab7 Control
Protrudin Control
Rab7 - Protrudin
D
Vehicle Control
Apilimod
YM-201636
Rab7 Control
KIF5B Control
Rab7 - KIF5B
E
PLA positive dots /cell
0.160
0.081
Vehicle Apilimod YM
Protrudin - VAPA
F
PLA positive dots /cell
0.014
0.044
Vehicle Apilimod YM
Rab7 - VAPA
G
PLA positive dots /cell
0.023
0.024
Vehicle Apilimod YM
Rab7 - Protrudin
H
PLA positive dots /cell
0.372
0.100
Vehicle Apilimod YM
Rab7 - KIF5B

FIGURE 7.

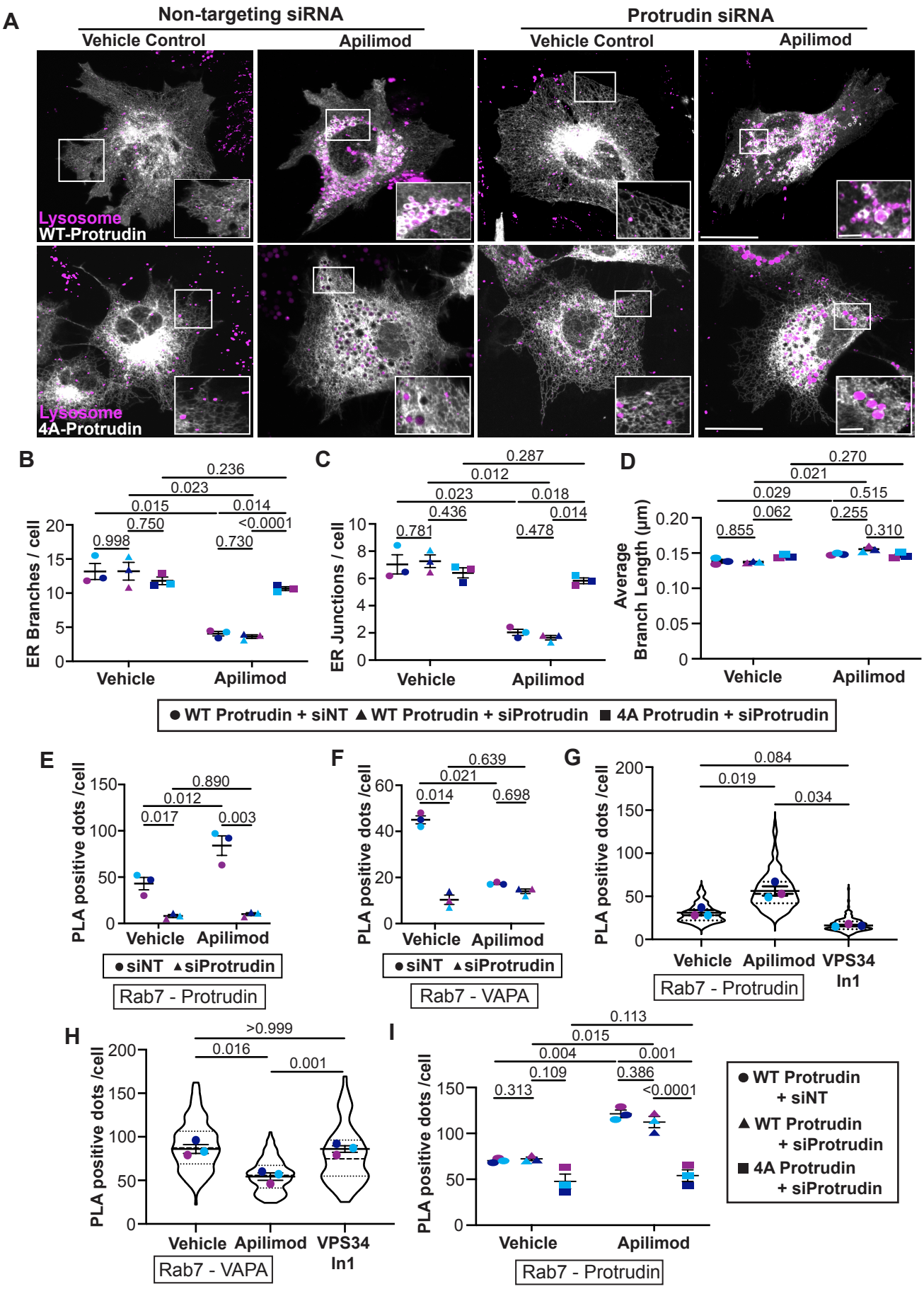
A
Non-targeting siRNA
Protrudin siRNA
Vehicle Control
Apilimod
Vehicle Control
Apilimod
Lysosome
WT-Protrudin
Lysosome
4A-Protrudin
B
ER Branches / cell
0.236
0.023
0.015
0.014
0.750
<0.0001
0.998
0.730
Vehicle
Apilimod
C
ER Junctions / cell
0.287
0.012
0.023
0.018
0.436
0.014
0.781
0.478
Vehicle
Apilimod
D
Average Branch Length (µm)
0.270
0.021
0.029
0.515
0.062
0.255
0.855
0.310
Vehicle
Apilimod
● WT Protrudin + siNT ▲ WT Protrudin + siProtrudin ■ 4A Protrudin + siProtrudin
E
PLA positive dots /cell
0.890
0.012
0.017
0.003
Vehicle
Apilimod
● siNT ▲ siProtrudin
Rab7 - Protrudin
F
PLA positive dots /cell
0.639
0.021
0.014
0.698
Vehicle
Apilimod
● siNT ▲ siProtrudin
Rab7 - VAPA
G
PLA positive dots /cell
0.084
0.019
0.034
Vehicle
Apilimod
VPS34 In1
Rab7 - Protrudin
H
PLA positive dots /cell
>0.999
0.016
0.001
Vehicle
Apilimod
VPS34 In1
Rab7 - VAPA
I
PLA positive dots /cell
0.113
0.015
0.004
0.001
0.109
0.386
0.313
<0.0001
Vehicle
Apilimod
Rab7 - Protrudin
● WT Protrudin + siNT
▲ WT Protrudin + siProtrudin
■ 4A Protrudin + siProtrudin